The CAGE Scanner: Development of a Novel Surface Event Rejection Technique in High Purity Germanium Detectors

Grace Song

A dissertation

submitted in partial fulfillment of the

requirements for the degree of

Doctor of Philosophy

University of Washington
2025

Reading Committee:
Jason Detwiler, Chair
Alejandro Garcia
Marilena Loverde

Program Authorized to Offer Degree:
Physics

University of Washington

Abstract

The CAGE Scanner: Development of a Novel Surface Event Rejection Technique in High Purity Germanium Detectors

Grace Song

Chair of the Supervisory Committee:

Jason Detwiler
Physics

The search for neutrinoless double beta ($0\nu\beta\beta$) decay aims to answer far-reaching questions about the nature of the neutrino mass, violation of lepton number conservation in the Standard Model, and the matter-antimatter asymmetry of the universe. The LEGEND experiment is pursuing this rare event search with the use of semiconductor detectors constructed of high-purity germanium, enriched in the candidate isotope ^{76}Ge. Precise understanding of detector response to radiation is crucial to the success of this experimental effort. This work describes the operation and improvement of the Collimated Alphas, Gammas, and Electrons (CAGE) Scanner, a test cryostat dedicated to the study of surface event behavior in different germanium detector geometries. Analysis of CAGE scans led to the development of a new pulse shape parameter, Early Charge (EQ), which is then applied to a subset of LEGEND-200 data to investigate its impact on LEGEND-200 backgrounds.

Acknowledgements

I couldn't have achieved any of this without the help of countless people. These are a small fraction of the mentors, peers, engineers, and friends who have supported me along the way.

I would like to thank my advisor, Jason Detwiler, for all of his mentorship, technical advice, and optimism throughout this program. I couldn't have asked for a more understanding advisor.

Many thanks to the LEGEND group postdocs, Clint Wiseman and Louis Varriano. Clint, for building CAGE from the ground up and for all of those long hours in the lab together. You made me feel welcome at CENPA during a pandemic that made it very strange to be working in lab at all. Louis, you manage to be brilliant and hardworking and kind all at once. I hope to have even a fraction of your competence one day.

The CENPA research staff and engineers were all so essential in this work. David Peterson, Tim Van Wechel, Tom Burritt, and Nate Miedema were always willing to help at a moment's notice with designing and testing new parts.

I also want to thank my friends, in particular Sanskriti Joshi, Sabrina Ang, Sam Borden, CJ Nave, Harry Ni, and Jimmy Sinnis, for the many hours at lunch, trivia nights, hiking, concerts, and even trips abroad that made graduate school so memorable.

I am so grateful to have the support of my family. My parents, Yufeng Li and Yafang Song, have always encouraged my curiosity and guided me through each stage of life. To my brother, Han, I've always been able to go to you for advice or to play a new video game, and now you've given me the cutest nephew alive.

Last but not least, I need to thank my partner, Amrit Amar. There's no one else I would rather have shared all the highs and lows of the past nine years with, and I couldn't have done it without you.

DEDICATION

To my cat, Arlo, who sat by my side from every first-year lecture to drafting this thesis, providing love and companionship every step of the way

Contents

List of Figures

List of Tables

Glossary

EQ_{tcorr} time-corrected value of EQoE.

μ_{period} error-weighted average value of EQoE over a period.

$0\nu\beta\beta$ **decay** Neutrinoless double beta decay.

A/E current/energy, risetime parameter.

BEGe broad energy germanium detector.

BSM beyond Standard Model.

CAGE Collimated Alphas, Gammas, and Electrons.

COAX coaxial detector.

DCR delayed charge recovery.

EQ early charge.

eq20 raw value of EQ taken at 20% time point.

EQ_Classifier final EQ parameter after energy correction.

EQoE "EQ over Energy", raw value of EQ normalized by energy.

FoM figure of merit.

HPGe high purity germanium.

ICPC inverted coaxial point contact detector.

IO inverted ordering.

MSE multi-site event.

NO normal ordering.

OPPI ORTEC prototype PPC investigation, PPC detector scanned in CAGE.

PEN polyethylene naphthalate.

PPC p-type point contact detector.

PSD pulse shape discrimination.

$Q_{\beta\beta}$ Q-value for $0\nu\beta\beta$ decay, $Q_{\beta\beta} = 2039$ keV in ^{76}Ge.

SSB spontaneous symmetry breaking.

SSE single-site event.

T/E max of triangle filter/energy, risetime parameter.

tp_x x% time point.

Chapter 1

Introduction

The Standard Model (SM) has been an incredibly powerful description of the universe as we observe it. It has successfully predicted the existence of new particles, such as the W, Z, and Higgs bosons, as well as made precision predictions of fundamental constants such as the electron dipole moment. Unfortunately, it also predicts that the universe should not exist. According to the Standard Model, matter and anti-matter were produced in equal amounts during the Big Bang, and there is no mechanism to produce an excess of matter over anti-matter. Yet today we observe structures much larger than the fundamental particles created in the Big Bang, from galaxies to planets to humans, that are all exclusively made up of matter, with minimal amounts of naturally occurring antimatter.

LEGEND is an experimental search for a beyond Standard Model (BSM) process known as neutrinoless double beta ($0\nu\beta\beta$) decay. $0\nu\beta\beta$ decay is a common prediction of models of the Big Bang that explain the observed matter-antimatter asymmetry of the universe. It all hinges on the properties of the least well-understood fundamental particle, the neutrino. In this chapter, I present a brief account of the puzzling history of the neutrino and describe how it has informed the theoretical motivations for the search for neutrinoless double beta decay.

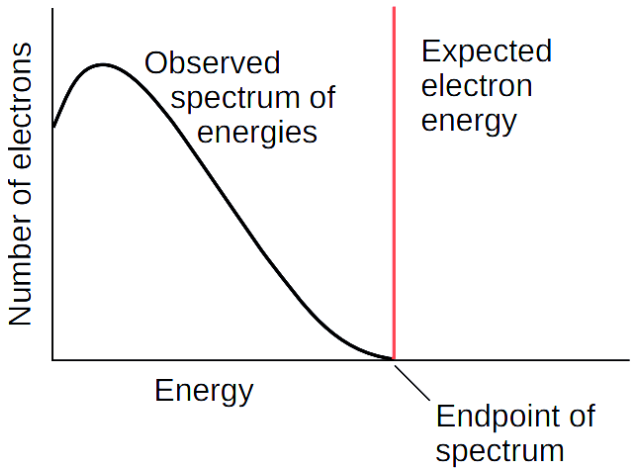

Figure 1.1: The observed beta decay spectrum (black) compared to the expected spectrum from "electron emission" (red) *Image Credit: Los Alamos Science*

1.1 History and Significance of the Neutrino

1.1.1 Motivations and Discovery

Nuclear beta decay is a process where an atomic nucleus converts one of its protons (neutrons) into a neutron (proton), emitting a positron (electron) and an electron (anti-)neutrino in the process. Before the existence of the neutrino was discovered, beta decay was thought to be purely "electron emission," where the final state consisted of only the new nucleus and an electron. In this case, the energy spectrum of the electron would be a monoenergetic line at the difference in mass of the initial and final state nuclei, or the Q-value of the decay. In 1914, when James Chadwick first measured this energy spectrum [1], he was baffled to find that it was a continuous spectrum, which seemed to violate energy conservation. The difference between the expected and observed spectra is shown in Fig. 1.1. Wolfgang Pauli was the first to propose a light, electrically neutral particle that may be emitted alongside the electron, carrying away some of the nuclear decay energy without being detected. This proposal was then formalized by Enrico Fermi, who coined the term "neutrino" [1].

It wasn't immediately obvious how to directly detect this hypothetical lepton with tiny mass and no charge. The first experimental observation of the neutrino was achieved more than twenty years later, in 1956, by Clyde Cowan Jr. and Frederick Reines in the Savannah River experiment [2]. This experiment sought to observe a process known as inverse beta decay, $\overline{\nu}_e + p \rightarrow n + e^+$, from an anti-neutrino source

on a water target to directly detect the existence of anti-neutrinos.

The theoretical prediction for the cross section of inverse beta decay on protons was 6.3×10^{-44} cm^2, so small that Hans Bethe called the process "practically unobservable," ([3]) and indeed, the best sensitivity of experiments of the time were seven orders of magnitude higher than this prediction. This exceedingly small cross section meant that Cowan and Reines needed a huge flux of anti-neutrinos to be sensitive to this process. Working at Los Alamos National Laboratory on nuclear testing, Cowan and Reines's first proposal was to use a nuclear bomb as an anti-neutrino source. Their detectors would need to be placed in an underground vacuum chamber near the explosion and dropped into free fall as the bomb was detonated to avoid being damaged by the shaking of the earth. The commissioning of this experiment went as far as beginning to drill the underground chamber before J.M.B. Kellogg convinced the pair to reconsider using a nuclear fission reactor instead of a nuclear bomb [2]. The use of reactors as neutrino sources was an important milestone in neutrino experiment, and many oscillation and coherent scattering experiments still use reactors as their source. The developments that allowed a nuclear fission reactor, with its much smaller anti-neutrino flux, to be competitive with a nuclear bomb include large liquid scintillator detectors and the use of time coincidence as a background rejection device, both of which are still used in neutrino experiments, such as LEGEND, today.

1.1.2 Neutrinos in the Standard Model

The Standard Model contains all free particle and interaction terms that obey local $SU(3) \times SU(2) \times U(1)$ gauge symmetry and Lorentz invariance. Each particle is represented by a field $\psi = \psi_L + \psi_R$ where ψ_L and ψ_R are the left and right chiral components of the field.

The neutrino, however, is unique among the fundamental fermions in that it doesn't require a right chiral component, $\nu = \nu_L$. Since neutrinos are electrically neutral leptons, they only interact through the weak force. The weak force has a unique property, discovered by C.S. Wu in 1957 [4], where it violates parity conservation by only coupling to a particle's left chiral component. This means that we have never observed a right-chiral neutrino, and do not need to include one in the Standard Model.

In order to reflect the structure of the gauge symmetries, fermions are arranged into left-handed doublets, whose components can transform into each other under weak interactions, and right-handed singlets that are

invariant under those weak interactions. For each generation, we get leptons that look like $L_L = \binom{\nu_L}{e_L}$ and e_R.

Masses for fermions are generated with Lagrangian terms $m(\overline{L_L} e_R + \overline{e_R} L_L)$. This can be interpreted as transitions between the left- and right-chiral components, with amplitude proportional to the mass of the particle. In general, fermions cannot form this term without violating $SU(2) \times U(1)$ gauge invariance, which is in conflict with the definitively observed fermion masses.

This problem was solved by the introduction of the Higgs field, $\Phi = \begin{pmatrix} \phi^+ \\ \phi^0 \end{pmatrix}$, whose interactions are described by a quartic potential,

$$V(\Phi) = -\mu^2 \Phi^\dagger \Phi + h(\Phi^\dagger \Phi)^2 \tag{1.1}$$

This is $SU(2) \times U(1)$ gauge invariant and has an infinite number of ground states, namely where $\Phi^\dagger \Phi = \frac{\mu^2}{2h} \equiv \frac{v^2}{2}$. As the universe cooled below a particular temperature, the Higgs field underwent spontaneous symmetry breaking and settled into one of those ground states, which we can choose to be the one with zero complex phase,

$$\Phi_0 = \begin{pmatrix} 0 \\ \frac{v}{\sqrt{2}} \end{pmatrix} \tag{1.2}$$

We can then redefine the Higgs field to be an expansion around such a ground state, so that

$$\tilde{\Phi} = \frac{1}{\sqrt{2}} \begin{pmatrix} 0 \\ v + H \end{pmatrix} \tag{1.3}$$

Introducing a Yukawa coupling between the Higgs and fermionic fields, $-y_f(\overline{L_L}\tilde{\Phi} e_R + \overline{e_R}\tilde{\Phi}^\dagger L_L)$, allows us to recover a mass term

$$\mathcal{L}_M = \frac{-y_f v}{\sqrt{2}}(\overline{L_L} e_R + \overline{e_R} L_L) \tag{1.4}$$

Coupling the neutrinos to the Higgs field would require the addition of a right-chiral singlet, so neutrinos remain massless in the Standard Model.

While only gauge symmetry and Lorentz invariance were required in the construction of the Standard Model, the Lagrangian contains multiple accidental symmetries that lead to accidentally conserved quantities: individual lepton numbers (L_e, L_μ, L_τ), total lepton number ($L = L_e + L_\mu + L_\tau$), total baryon number

Parameter	Normal Ordering	Inverted Ordering
$\sin^2(\theta_{12})$	0.307 ± 0.013	0.307 ± 0.013
$\sin^2(\theta_{23})$	$0.547^{+0.018}_{-0.024}$	$0.534^{+0.021}_{-0.024}$
$\sin^2(\theta_{13})$	$(2.20 \pm 0.07) \times 10^{-2}$	$(2.20 \pm 0.07) \times 10^{-2}$
δ_{CP}	$1.23 \pm 0.21\pi$	$1.23 \pm 0.21\pi$
Δm^2_{21}	$(7.53 \pm 0.18) \times 10^{-5} eV^2$	$(7.53 \pm 0.18) \times 10^{-5} eV^2$
Δm^2_{32}	$(2.437 \pm 0.033) \times 10^{-3} eV^2$	$(-2.519 \pm 0.033) \times 10^{-3} eV^2$

Table 1.1: Most precise measurements of the oscillation parameters in the PMNS matrix, for both the normal and inverted orderings. Data taken from the PDG [5].

(B), $B + L$, and $B - L$. Since these conservation laws are not fundamental, processes that break them are promising candidates for new physics. For example, sphaleron processes are a non-perturbative process that change B and L by three units each, violating B, L, and $B + L$ but leaving $B - L$ conserved. These processes could convert an anti-lepton excess in the early universe to the baryon excess we currently observe. This motivates a search for leptogenic processes in order to explain the matter-antimatter asymmetry of the universe.

1.2 Neutrino Mass

1.2.1 Neutrino Oscillation

A first hint of new physics in the neutrino sector came from the solar neutrino anomaly. The Homestake experiment in 1965 aimed to detect electron neutrinos produced in the sun to confirm that solar fusion behaved according to the standard solar model. However, they only detected a third of the electron neutrinos they expected [6]. In the 1980s, results from IMB [7] and Kamiokande [8] detected an absence of atmospheric muon neutrinos from cosmic ray showers. It wasn't until Superkamiokande in 1998 [9], the SNO experiment in 2001 [10], and KamLAND in 2004 [11] that the required sensitivity was reached to confirm neutrino oscillation was responsible for these anomalies. This discovery requires neutrinos to have a non-zero mass. Neutrino oscillation arises from mixing between the mass eigenstates, which are responsible for neutrino propagation, and the flavor eigenstates, which couple neutrinos to the charged leptons in weak interactions, such as production through beta decay or charged-current scattering.

Solar neutrinos, for example, are produced entirely in the weak electron neutrino eigenstate, ν_e. This

can be written in the mass eigenbasis as a combination of three mass eigenstates,

$$|\nu_e\rangle = U_{e1}\,|\nu_1\rangle + U_{e2}\,|\nu_2\rangle + U_{e3}\,|\nu_3\rangle \tag{1.5}$$

where U_{e1}, U_{e2}, and U_{e3} are complex mixing parameters for each mass eigenstate. The same can be said for ν_μ and ν_τ, each with their own mixing parameters. These three statements can be combined into

$$\begin{pmatrix} \nu_e \\ \nu_\mu \\ \nu_\tau \end{pmatrix} = \begin{pmatrix} U_{e1} & U_{e2} & U_{e3} \\ U_{\mu 1} & U_{\mu 2} & U_{\mu 3} \\ U_{\tau 1} & U_{\tau 2} & U_{\tau 3} \end{pmatrix} \begin{pmatrix} \nu_1 \\ \nu_2 \\ \nu_3 \end{pmatrix} \tag{1.6}$$

This mixing matrix between the flavor and mass eigenstates of neutrinos is known as the Pontecorvo-Maki-Nakagawa-Sakata (PMNS) matrix. As it is a 3x3 unitary matrix, it requires 9 free parameters to be fully described. 3 of these parameters are phases that can be absorbed into a redefinition of the leptonic fields, leaving us with 6 physical parameters. These are often described by

$$U_{PMNS} = \begin{bmatrix} 1 & 0 & 0 \\ 0 & c_{23} & s_{23} \\ 0 & -s_{23} & c_{23} \end{bmatrix} \begin{bmatrix} c_{13} & 0 & s_{13}e^{-i\delta_{\mathrm{CP}}} \\ 0 & 1 & 0 \\ -s_{13}e^{i\delta_{\mathrm{CP}}} & 0 & c_{13} \end{bmatrix} \begin{bmatrix} c_{12} & s_{12} & 0 \\ -s_{12} & c_{12} & 0 \\ 0 & 0 & 1 \end{bmatrix} \begin{bmatrix} e^{i\alpha_1/2} & 0 & 0 \\ 0 & e^{i\alpha_2/2} & 0 \\ 0 & 0 & 1 \end{bmatrix} \tag{1.7}$$

where $c_{ij} = \cos\theta_{ij}$, $s_{ij} = \sin\theta_{ij}$. This gives the six free parameters as three mixing angles between the mass eigenstates, θ_{12}, θ_{23}, and θ_{13}, one phase associated with CP violation, δ_{CP}, and two phases that are only physical if the neutrino is Majorana, α_1 and α_2. The possible Majorana nature of the neutrino is discussed in Sec. 1.3.1. The most precise measurements of each of these parameters to date is given in Table 1.1.

Neutrino oscillation experiments measure the transition probability between different neutrino flavor eigenstates. In a model which only considers contributions from two neutrino flavors and propagation through vacuum, this probability is proportional to $\sin^2(\Delta m^2_{ij})$, where $\Delta m^2_{ij} = m^2_i - m^2_j$ are the differences in the squared eigenmasses [12]. The measured values, reported in Table 1.1, show that Δm_{32} is larger than Δm_{21} by a factor of ~ 30. This is indifferent to the sign of Δm_{ij}. From solar ($\nu_e \to \nu_\mu$) and atmospheric

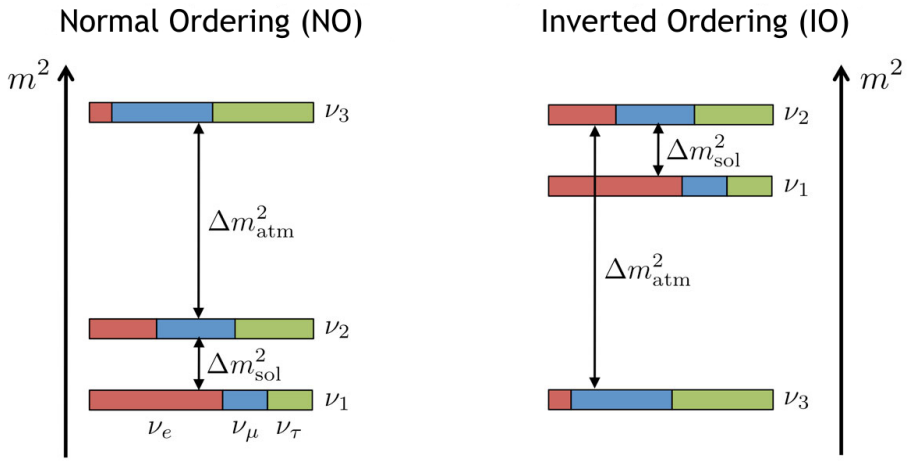

Figure 1.2: Visualization of the two possible neutrino mass hierarchies. *Image Credit: Hitoshi Murayama*

($\nu_\mu \rightarrow \nu_\tau$) neutrino oscillation experiments, we measure Δm^2_{sol} and Δm^2_{atm}. However, the oscillation pattern of solar neutrinos are impacted by the MSW effect, which accounts for flavor transformation of neutrinos as they exit the dense matter of the sun. The MSW effect is impacted by the sign of the difference, meaning we can determine $\Delta m^2_{21} > 0$, but the sign of Δm_{31} and Δm_{32} are unknown. This is known as the mass hierarchy problem, as we can measure the two mass splittings, but we can't determine the order of the masses. Either $m_1 < m_2 < m_3$, which is known as the normal ordering (NO), or $m_3 < m_1 < m_2$, which is known as the inverted ordering (IO). These two possibilities are visualized in Fig. 1.2. In either case, the lightest neutrino mass is still allowed to be zero, as oscillation experiments are not sensitive to the absolute scale of the neutrino masses. The real ordering will affect the sensitivity required to detect $0\nu\beta\beta$ decay, which is discussed more in Section 1.4.3. Next generation oscillation experiments, such as DUNE[13], HyperKamiokande [14], and JUNO [15], should be sensitive to the effects of propagation through matter and be able to make a determination between NO and IO.

It is interesting to note that the discovery of neutrino oscillation violates the conservation of individual lepton number, one of the accidental symmetries of the Standard Model discussed in Section 1.1.2. This suggests that the neutrino sector could be a promising place to search for processes that break the last remaining accidental symmetry, $B - L$.

1.3 Nature of Neutrino Mass

1.3.1 Majorana Particles

At the heart of the mystery surrounding the nature of neutrino mass lies the question of whether neutrinos are Majorana or Dirac. Before discussing the specific mechanisms to generate a neutrino mass, we must draw a distinction between Dirac and Majorana particles and why it matters.

All fermions, Dirac and Majorana, satisfy the Dirac equation

$$(i\partial\!\!\!/ - m)\psi = 0 \tag{1.8}$$

The general solution ψ to the Dirac equation is a 4-component bispinor, which can be written in terms of its left and right chiral components, $\psi = \psi_L + \psi_R$. This contains four independent degrees of freedom, corresponding to a left-chiral particle, right-chiral antiparticle, right-chiral particle, and left-chiral antiparticle.

A Majorana particle is a solution to the Dirac equation that can be written as only a 2-component spinor. Ettore Majorana figured out that such a particle could exist if we set the right-chiral particle to be the charge conjugate of the left-chiral antiparticle, $\psi_R = C\overline{\psi_L}^T$ [16]. If we then apply the charge conjugation operator to the entire Dirac spinor, we find

$$\psi^c = \overline{C(\psi_L + C\overline{\psi_L}^T)}^T = C\overline{\psi_L}^T + \psi_L = \psi \tag{1.9}$$

i.e. that a Majorana particle is its own antiparticle. Its two degrees of freedom correspond to a left-chiral "thing" and a right-chiral "thing", with no distinction between particles and antiparticles. This requires that the left and right chiral components have the same quantum numbers, implying that Majorana particles must be electrically neutral.

1.3.2 Dirac vs. Majorana Mass

Measurements of neutrino oscillation tell us that at least two of the neutrino masses are non-zero. The next step would then be determining how to modify the Standard Model Lagrangian to include a mass term for the neutrinos. One natural way would be to include a sterile right handed neutrino singlet, ν_R, so that the

neutrino obtains a Dirac mass through the same Higgs mechanism as the other fermions. This would insert a term

$$\mathcal{L} \supset \frac{-y_\nu v}{\sqrt{2}}(\overline{L_L}\nu_R + \overline{\nu_R}L_L) \tag{1.10}$$

This leads us to discuss two oddities about the neutrino mass that differentiates it from the other fermion masses.

First, measurements of the tritium β decay spectrum by KATRIN [17] place an upper limit on a PMNS-weighted average of the neutrino masses of 0.45 eV. This leaves a gulf of six orders of magnitude between the neutrino masses and other fermion masses, and leads us to question why the same mass generation mechanism would produce two sets of masses at such different energy scales with nothing in between. While there is nothing theoretically wrong with this, it brings many physicists a sense of unease that motivates an alternative explanation.

Second, the introduction of a right handed singlet for the neutrino iw well motivated by Grand Unifcation efforts that extend the gauge symmetry of the Standard Model to, for example, $SO(10)$. With this new singlet, combined with the fact that the neutrino is electrically neutral, we are allowed to form the term

$$\mathcal{L} \supset m_R\overline{\nu_R^c}\nu_R = m_R\nu_R^T C\nu_R \tag{1.11}$$

An analogous term for the existing left-handed neutrino could not have been formed, as it would have an overall weak hypercharge of -2, violating gauge symmetry. This coupling of a particle to its charge conjugate is called the Majorana mass term, and it violates conservation of lepton number and $B - L$ by 2 units. Since these are only accidentally conserved quantities in the Standard Model, there is no reason to exclude this term from the Lagrangian. To make neutrinos strictly Dirac particles and eliminate the right-handed Majorana mass term from the Lagrangian, we need to find a symmetry that elevates $B - L$ to a fundamentally conserved quantity of the Standard Model.

1.3.3 Seesaw Mechanism

With both the spontaneous symmetry breaking of the Higgs and the Majorana mass term, our neutrino mass terms can be written generically as

$$\mathcal{L}_{m_\nu} = \frac{1}{2} N_L^T C^\dagger M N_L + \text{h. c.} \tag{1.12}$$

$$N_L = \begin{pmatrix} \nu_L \\ C\overline{\nu_R}^T \end{pmatrix}, M = \begin{pmatrix} 0 & m_D \\ m_D & m_R \end{pmatrix} \tag{1.13}$$

where $m_D = \frac{y_\nu v}{\sqrt{2}}$ is the Dirac mass. It should be noted that we will continue to use just one neutrino generation for illustrative purposes, but including all 3 generations would cause m_D and m_R to become 3×3 matrices, and ν_L, ν_R would be vectors of 3 bispinors.

If we assume that the sterile right-handed neutrino is much heavier than the SM neutrino, we can diagonalize the mass matrix to get two eigenmasses, $m_1 \sim \frac{m_D^2}{m_R}$ and $m_2 \sim m_R$. As m_R increases, m_1 gets smaller. This relationship is called the type I seesaw mechanism, and it provides a natural explanation for why the observed neutrino masses are so small by introducing new physics at high energy scales. If the Yukawa coupling is $\mathcal{O}(1)$, as it is for the top quark, and we consider the upper limits for the neutrino mass from β decay experiments, that gives a scale for $m_R \sim 10^{15}$ GeV. This is tantalizingly similar to the GUT scale, where the electromagnetic, weak, and strong forces unify, theorized to be $\sim 10^{16}$ GeV.

Even without those specific assumptions, the type I seesaw mechanism is alluring because of the introduction of the heavy right-handed neutrino. In a theory known as thermal leptogenesis, a CP-violating decay of this neutrino in the early universe generates a lepton-antilepton asymmetry [18]. This lepton asymmetry would then be converted into a baryon asymmetry by the non-perturbative sphaleron processes mentioned in Section 1.1.3. A right-handed Majorana neutrino could explain the currently observed baryon excess with masses as low as $m_R > \mathcal{O}(10\text{ GeV})$ [19].

The fact that the previously discussed mechanism is called the type I seesaw mechanism heavily implies the existence of a type II seesaw mechanism. The type II seesaw mechanism does not introduce a right-handed neutrino, but rather allows us to form the Majorana mass term with the SM left-handed neutrino. In the previous section, I stated that this wasn't possible due violation of $SU(2) \times U(1)$ gauge symmetry. This

is overcome with the addition of a new Higgs triplet field, Δ, in addition to the SM Higgs, Φ.

$$\Delta = \begin{pmatrix} \delta^+/\sqrt{2} & \delta^{++} \\ \delta^0 & -\delta^+/\sqrt{2} \end{pmatrix} \tag{1.14}$$

This allows the left-chiral lepton to be coupled to itself without violating weak hypercharge conservation, and similarly to how spontaneous symmetry breaking of the SM Higgs field led to Dirac masses for fermions, the spontaneous symmetry breaking of the Δ field gives rise to Majorana masses for the left-handed neutrinos, $m_\nu \sim y|\mu|v^2/(2m_\Delta^2)$. This model can also explain the observed baryon asymmetry and < 1 eV scale of the neutrino masses with a Higgs triplet mass of at least 1 TeV [20].

There is even a third seesaw mechanism, unsurprisingly termed the type III seesaw mechanism. Like the type I seesaw, this mechanism introduces a new fermion, N, but as a triplet like the type II seesaw instead of a singlet. The Majorana masses are then generated in a similar fashion to the type I seesaw, with the large mass of the new fermion forcing the neutrino mass to be small.

1.3.4 Weinberg Operator

The Majorana mass term is also motivated by the framing of the Standard Model as the low energy limit of a higher dimensional grand unified theory. The accidental symmetries of the SM may be broken at higher energy scales, and only appear to be conserved at low energies. The Standard Model Lagrangian contains terms up to dimension-4, so the lowest order effects of this GUT would come in as a dimension-5 operator. There is only one dimension-5 operator that is can be constructed from SM fields, and it is known as the Weinberg operator [21].

$$\mathcal{L}_5 = \frac{c_5}{\Lambda}(\overline{L_L} \cdot \Phi)(\Phi^T \cdot L_L^c) \tag{1.15}$$

where c_5 is some coupling constant and Λ describes the energy scale where the dimension-5 operator becomes relevant. It is interesting to note that this operator violates lepton number conservation by two units, implying that lepton number is not a fundamental symmetry of the SM, but rather a symmetry that is only

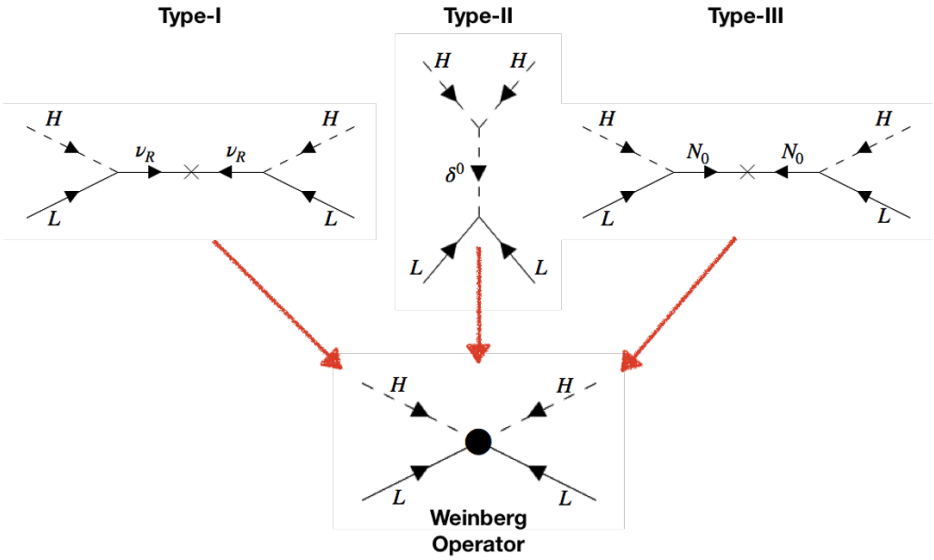

Figure 1.3: The three seesaw mechanisms are depicted above, with their respective heavy internal propagators, ν_R, δ^0, and N_0. When those are integrated out at low energies, they each result in the Weinberg operator. *Image Credit: [22]*

conserved at low energies. After electroweak symmetry breaking, this term becomes

$$\frac{c_5}{\Lambda}\overline{L_L^c}L_L$$

which connects the left-handed neutrino to its charge conjugate, a.k.a. a Majorana mass term. The different seesaw mechanisms described in the previous section all generate the Weinberg operator when the heavy degrees of freedom are integrated out, demonstrated in Fig. 1.3, and only differ in the values for c_5 and Λ.

The leading order BSM term manifests at low energies as a Majorana mass term for the neutrino. This is agnostic to any underlying theory that generates this term, though it is consistent with all the seesaw mechanisms that can be used to explain the scale of the observed neutrino mass and the baryon asymmetry of the universe. While it is possible to construct models without this term, there is no current motivation for including higher order terms and excluding the dimension-5 term.

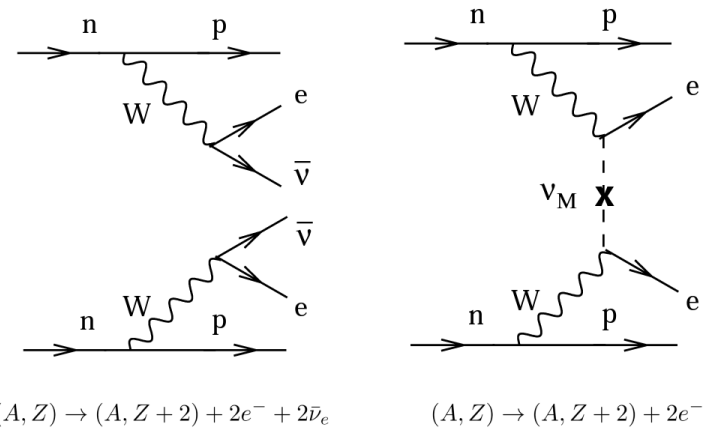

Figure 1.4: Feynman diagram and decay equation for (*left*) $2\nu\beta\beta$ and (*right*) $0\nu\beta\beta$. *Image Credit: [23]*

1.4 Neutrinoless Double Beta Decay

1.4.1 What Is It

So far we've outlined why the observation of neutrino oscillation has raised interesting questions about the Majorana nature of neutrino masses and how the answer to that question can shed light on fundamental symmetries, new physics at high energies, and the baryon asymmetry of the universe. To probe this question experimentally, the most promising observable signature lies in the search for $0\nu\beta\beta$ decay.

$0\nu\beta\beta$ decay can be contrasted with two neutrino double beta decay, where two regular beta decays occur simultaneously, emitting two electrons and two electron antineutrinos (or two positrons and two electron neutrinos). This is a rare Standard Model process that has been observed in a handful of nuclei with a lifetime of $10^{18} - 10^{21}$ years [5].

In $0\nu\beta\beta$ decay, the neutrinos remain virtual as one of the antineutrinos can be absorbed as a neutrino by the other nucleon in a process known as light neutrino exchange, shown in Fig. 1.4, emitting just the two final state electrons. This process is beyond the Standard Model because it violates lepton number conservation, and its observation would imply that a Majorana mass term for neutrinos should be added to the SM Lagrangian.

It should be noted that light neutrino exchange is not the only possible mediator of $0\nu\beta\beta$ decay. The BSM theories that resolve the baryogenesis problem through leptogenesis, Majorana neutrino masses, the

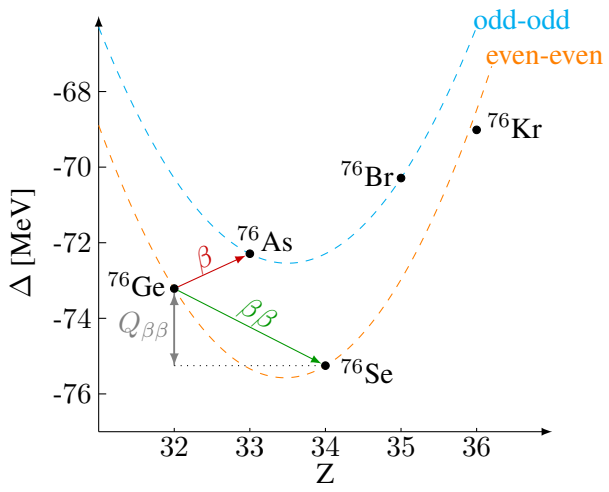

Figure 1.5: The mass excess, $\Delta = m - A$, is depicted for isobars with mass number $A = 76$, with odd-odd nuclei lying on the upper blue curve and even-even nuclei on the lower orange curve. *Image credit: [21]*

Weinberg operator, and seesaw mechanisms, however, all generally predict the existence of $0\nu\beta\beta$ decay. Regardless of the underlying mechanism, a successful observation would demonstrate the violation of lepton number conservation and imply the Majorana nature of the neutrino.

1.4.2 How to Observe It

In most nuclei, single beta decay would present an overwhelming and irreducible background for both types of $\beta\beta$ decay. However, there exist certain even-even nuclei (A, Z) where single beta decay is energetically forbidden to their odd-odd $(A, Z+1)$ neighbors, but double beta decay is permitted to the even-even $(A, Z+2)$ nucleus. These allowed and forbidden transitions for the nucleus of ^{76}Ge and its surrounding nuclei is shown in Fig. 1.5.

$2\nu\beta\beta$ decay is an irreducible background in the search for $0\nu\beta\beta$ decay. An obvious difference in their experimental signatures would be the detection of the outgoing antineutrinos. Neutrinos are so loathe to interact with the outside world, however, that it is not experimentally feasible to detect those outgoing neutrinos with a great enough efficiency to be confident that the lack of detection means an actual lack of neutrinos. Instead, it is much easier to detect the outgoing electrons. In $2\nu\beta\beta$ decay, the electrons share the final state energy with the neutrinos, so they are emitted in a continuous spectrum of energies up to $Q_{\beta\beta} - 2m_\nu$. Without the emission of neutrinos, $0\nu\beta\beta$ decay behaves like the "electron emission" that was

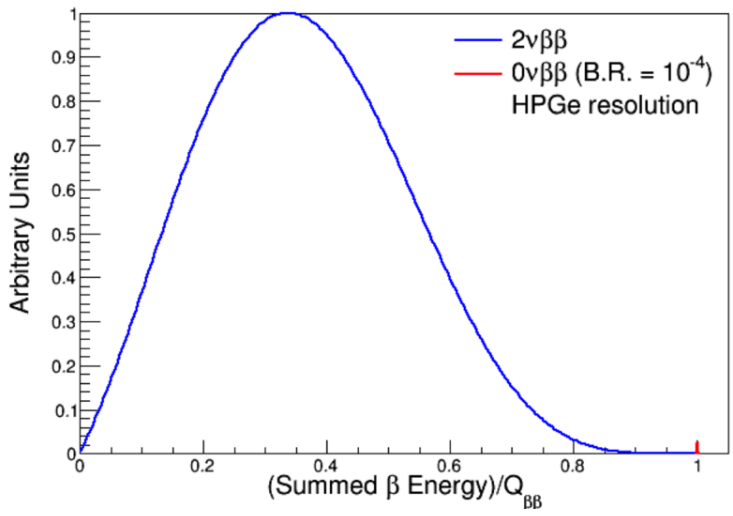

Figure 1.6: The expected experimental signature of the $2\nu\beta\beta$ decay spectrum and peak from $0\nu\beta\beta$. The peak has been enlarged by a factor of 10 over existing limits for visibility. *Image Credit: Jason Detwiler*

expected of single beta decay, and the electrons carry away the entire $Q_{\beta\beta}$ energy of the decay, resulting in a monoenergetic peak at the end of the $2\nu\beta\beta$ decay spectrum. In order to resolve such a peak, the main considerations for experimental design are the suppression of external background radiation and detector energy resolution. The expected signal for an ideal experiment with zero external background and the energy resolution demonstrated in germanium detectors is shown in Figure 1.6.

The techniques used to minimize background and improve energy resolution are largely determined by an experiment's choice of isotope. A partial list of isotopes currently used in $0\nu\beta\beta$ decay searches can be found in Table 1.2. A higher value of $Q_{\beta\beta}$ allows searches to sit above naturally occurring radiation, requiring less radiopure materials and background shielding to reach the background-free regime. A higher natural abundance, in general, means it will be more affordable to acquire large amounts of the candidate isotope, allowing more exposure in less time. However, this needs to be considered along with the cost of enriching material in the candidate isotope and the existence and availability of industrial processes to perform the enrichment. The isotope will also affect the kinds of detector technologies that can be used in conjunction with that isotope, which will affect energy resolution and viability of different background rejection procedures. LEGEND uses ^{76}Ge as its candidate isotope. The relatively low $Q_{\beta\beta}$ and natural abundance are offset by its great energy resolution, well-developed background rejection techniques, and established enrichment procedures.

Isotope	$Q_{\beta\beta}$ [keV]	Natural Abundance [%]	Achievable Enrichment [%]
^{76}Ge	2039.061(7)	7.75(12)	92
^{82}Se	2997.9(3)	8.82(15)	96.3
^{100}Mo	3034.40(17)	9.744(65)	99.5
^{130}Te	2527.518(13)	34.08(62)	92
^{136}Xe	2457.83(37)	8.857(72)	90

Table 1.2: Partial list of isotopes used in $0\nu\beta\beta$ decay searches, along with some of the factors that affect isotope selection. Values from [21].

1.4.3 Limits and Outlook

To quantify the expected lifetime of $0\nu\beta\beta$ decay, we focus on light neutrino exchange as the underlying mechanism. The expected decay rate for this process is given by

$$(T^{0\nu})^{-1/2} = G_{01} g_A^4 \mathcal{M}^2 \frac{m_{\beta\beta}^2}{m_e^2} \tag{1.16}$$

The parts of this equation are

- G_{01}: the phase space factor that captures the kinematics of the decay
- g_A: the axial current coupling constant
- $\mathcal{M}$: the nuclear matrix element describing the transition amplitudes between initial and final state nuclei
- $m_{\beta\beta}$: the effective Majorana mass, described by

$$m_{\beta\beta} = \left| \sum_{i=1}^{3} |U_{ei}|^2 e^{i\alpha_i} m_i \right| \tag{1.17}$$

  where U_{ij} is the PMNS matrix and α_i are the Majorana phases discussed in Section 1.2.1.

We can see that the decay rate scales with $m_{\beta\beta}^2$, so the tiny neutrino masses mean that this is an extremely rare process.

Given that the Majorana phases are not measurable by oscillation experiments, we expect some uncertainty in the decay rate. The largest uncertainty, however, actually comes from the nuclear matrix elements,

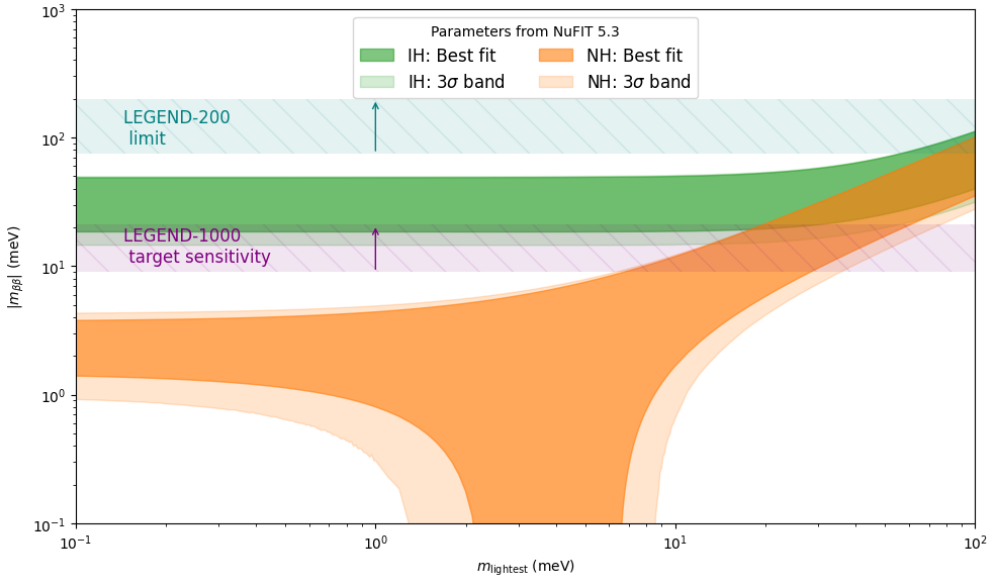

Figure 1.7: The allowed phase space for the effective Majorana mass as a function of the lightest neutrino mass for the normal and inverted orderings. The current best limit from experiment is shown as a blue band, with limits for specific isotopes in the inset. The expected sensitivity for ton-scale experiments is shown in pink. *Image Credit: Jorge Torres, LobsterPlot package*

due to the complicated many-body physics in heavy nuclei. However, recent developments in *ab initio* computational methods have provided promising results for reducing the uncertainty on these terms in the near future [21].

Measurements of the PMNS matrix from oscillation experiments allow us to make predictions on $m_{\beta\beta}$ as a function of the lightest neutrino mass. This means that the predictions are dependent on the neutrino mass hierarchy, as either m_1 or m_3 will be the lightest. These predictions are presented in Figure 1.7. The lifetimes to which current experiments are sensitive can be converted to upper limits on $m_{\beta\beta}$. The current best limit on the half-life is 2.3×10^{26} years in ^{136}Xe and 1.8×10^{26} years in ^{76}Ge. The next generation of ton-scale experiments, including LEGEND-1000, are expected to fully cover the IO parameter space [21].

Chapter 2

LEGEND Overview

The largest experimental challenges in the search for $0\nu\beta\beta$ decay are energy resolution and minimizing radioactive backgrounds. For the best energy resolution, LEGEND uses ^{76}Ge ($Q_{\beta\beta} = 2039.06$ keV) as its candidate isotope, allowing the use of high-purity germanium (HPGe) semiconductor detectors as both source and detector. These detectors have demonstrated an energy resolution of 0.12% FWHM at $Q_{\beta\beta}$, the best of any $0\nu\beta\beta$ decay search[24].

LEGEND uses three main techniques for reducing external backgrounds: passive shielding, active shielding, and pulse shape discrimination (PSD).

Passive shielding encompasses the ways that natural radiation can be removed from the experiment. LEGEND is located at Gran Sasso National Laboratory (LNGS), which sits underneath the Gran Sasso Mountain range, providing 3700 m.w.e. of radiation shielding [25]. LEGEND also utilizes underground electroformed copper for support structures and custom low mass front end electronics, minimizing the amount of material near the detector, which could introduce radioactive backgrounds.

Active shielding is the inclusion of an additional detector system to tag external radiation. Those background events can then be removed from dataset, even if that radiation does enter the active volume. LEGEND uses multiple layers of active shielding. First, a water tank is outfitted with photomultiplier tubes (PMTs) to detect Cherenkov light from muons. Then, the germanium detectors are submerged in a liquid argon (LAr) cryostat, which both cools the germanium detectors to operating temperature and scintillates in response to ionizing radiation. The germanium detectors sit on polyethylene naphthalate (PEN) baseplates

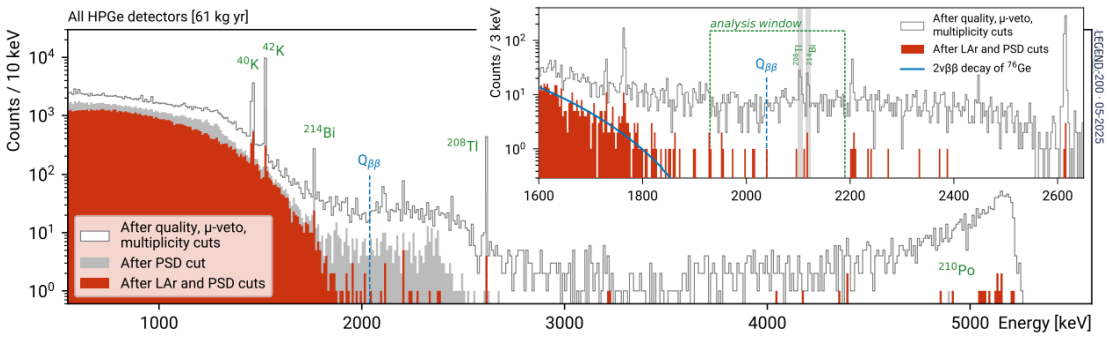

Figure 2.1: Energy spectrum of LEGEND-200's first data release. The hollow grey histogram shows the events surviving muon veto, quality, and multiplicity cuts. The solid grey histogram shows the events after PSD cuts, and the red histogram shows the events after both the PSD cuts and liquid argon veto. [26]

which also scintillate. The scintillation light is captured by wavelength shifting (WLS) fibers and funneled into silicon photomultipliers (SiPMs) to detect the light. The fiber curtains improve the geometric coverage and shift the scintillation light into green wavelengths to maximize the detection efficiency of the SiPMs. Any germanium events which are time-coincident with events in the muon or LAr vetos that exceed an established threshold are excluded from the final analysis.

The final background mitigation technique is a process known as pulse shape discrimination. This is an analysis technique that identifies the characteristics of incident radiation via the signals it produces. This allows events that do not share characteristics with $0\nu\beta\beta$ decay to be excluded from the final dataset. A more detailed discussion on PSD techniques currently used in LEGEND is in 2.3 and the contribution of this work to PSD techniques is in Chapters 4 and 5.

The LEGEND experiment is being commissioned in a phased approach. LEGEND-200, with a goal of 200kg of germanium detectors, is currently operating at LNGS. First results with 61 kg yr of data were published, which when combined with data from its predecessor experiments, provides the world-leading limit on the $0\nu\beta\beta$ decay half-life in ^{76}Ge, $T_{1/2} > 1.9 \times 10^{26}$ yrs [26]. LEGEND-200 also serves as a demonstration of the feasibility of scaling to the next-generation experiment, LEGEND-1000. With 1000 kg of germanium, LEGEND-1000 aims to reach sensitivities of $T_{1/2} > 10^{28}$ yrs, probing the entire parameter space covered by the inverted ordering of neutrino masses [21].

The current performance of LEGEND-200 shows that the PSD cuts and the LAr veto are equally responsible for bringing the experiment to a quasi-background free regime. In Figure 2.1, the energy spectrum from

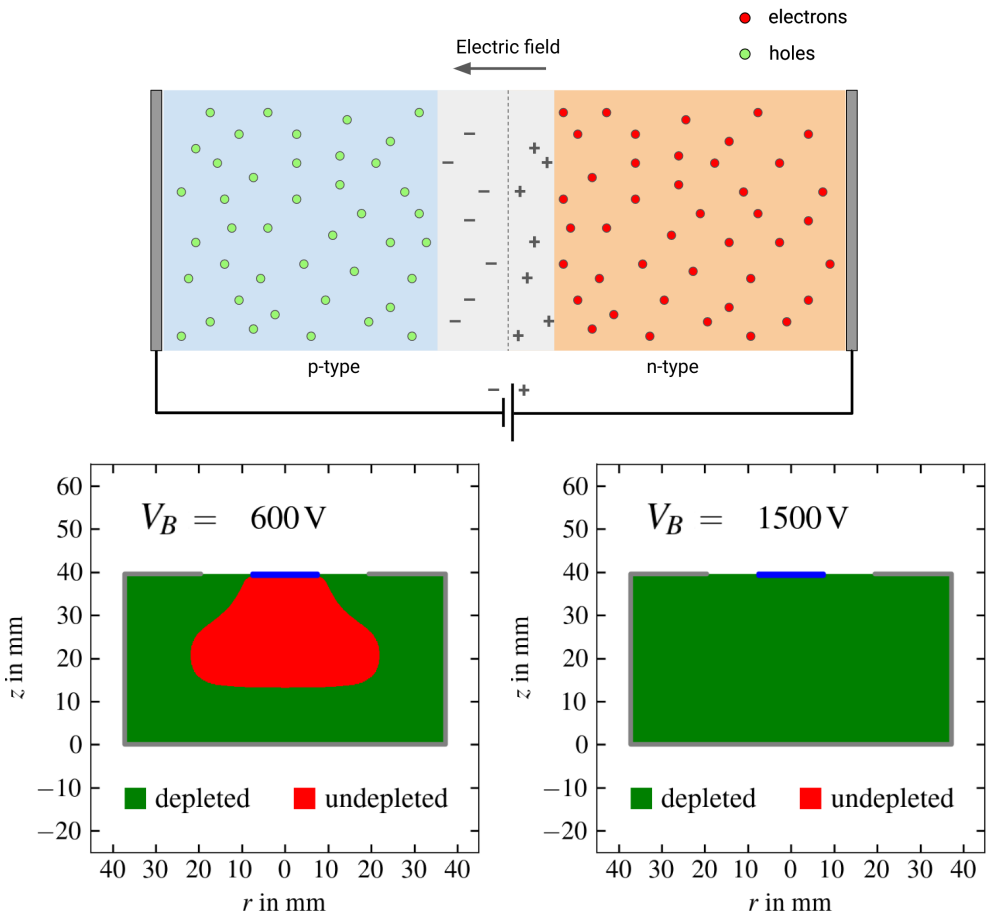

Figure 2.2: *(top)* Illustration of a p-n junction and the initial formation of a depletion region. A voltage is applied across the device to expand the depletion region. *(bottom)* Simulations of partial and full depletion of a germanium detector. The detector begins depleting near the n+ high voltage contact (shown in grey), and moves inwards as more voltage is applied, until the entire detector is depleted. *Image credit: Felix Hagemann*

one year of data-taking with LEGEND-200 is shown [26]. Near the region of interest, the liquid argon veto and pulse shape discrimination are each responsible for approximately one order of magnitude reduction in background.

2.1 HPGe Detectors

High purity germanium (HPGe) detectors are semiconductors that detect radiation through the creation and drift of electron-hole pairs. They operate as a reverse-biased p-n junction. The bulk of the detector is

intrinsic germanium, with a p+ boron implanted contact in a central dimple, and an n+ lithium diffused contact on the outer surfaces. When the electrically neutral p+ and n+ surfaces are in contact, the excess valence electrons in the n+ material drift towards the excess holes in the p+ material. This creates regions of negative charge in the p+ material and positive charge in the n+ material, establishing an electric field directed towards the p+ contact. This region of non-zero electric field is called the *depletion region* of the detector. An external high voltage is then applied to the n+ contact while the p+ contact is held at ground to expand this depletion region until the entire detector is depleted (see Figure 2.2 for a visualization of the depletion process). To maintain this voltage difference, the n+ and p+ contacts are separated by a layer of insulating amorphous Ge called the *passivated surface*, which results in a dead layer $\mathcal{O}(10)$ μm thick [27]. When radiation deposits energy in the depletion region region, valence electrons are promoted into the conduction band of the semiconductor, creating electron-hole pairs that are free to drift in the electric field. The number of generated electron-hole pairs is proportional to the deposited energy of the incident event. In germanium, it takes an average of 2.96 eV [28] to create an electron-hole pair. The holes drift towards the p+ contact and the electrons drift towards the n+ contact. This moving charge creates a detectable signal, following the Shockley-Ramo theorem

$$Q_{ind} = q\Delta\phi \tag{2.1}$$

where Q_{ind} is the charge induced on the p+ contact, q is the drifting charge, and $\Delta\phi$ is the change in weighting potential that the charge experiences along its drift path. This induced charge is collected on a feedback capacitor connected to the p+ contact, and the voltage across the capacitor is measured as our signal, shown in Fig. 2.3.

The number of generated electron-hole pairs, proportional to the energy deposited in the detector, determines the height, and the drift time of the charges determines the rise time of the signal. In order to reset the electronics for continuous operation, the charge induced on the readout electronics is discharged by a feedback resistor in parallel with the feedback capacitor. This allows the signal to exponentially decay down to the detector baseline until a new event arrives. These decay times are $\mathcal{O}(100)$ μs, much longer than the rise times of $\mathcal{O}(1)$ μs.

The weighting potential is solely determined by the geometry of the detector. LEGEND-200 uses a mix

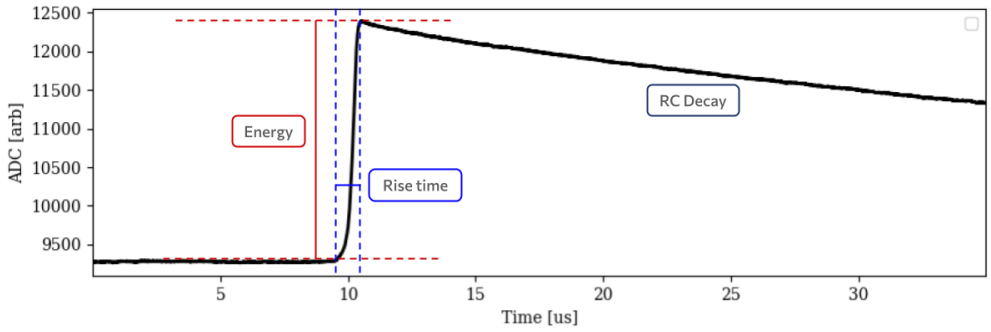

Figure 2.3: The signal produced in germanium due to incident radiation.

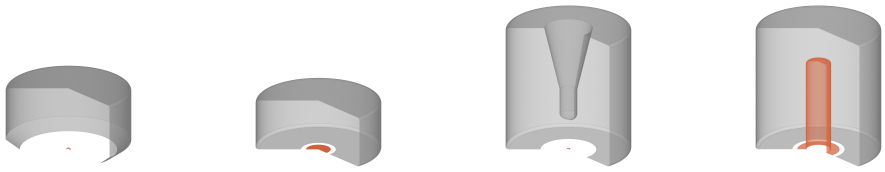

Figure 2.4: The detector geometries found in LEGEND-200, from left right: PPC, BEGe, ICPC, and Coax. The p+ contacts are shown in orange, n+ contacts in grey, and the white gaps between the contacts represent the passivated surface. LEGEND-1000 will exclusively deploy ICPC detectors. *Image Credit: David Hervas*

of four geometries, pictured in Figure 2.4. The coaxial geometry, which was inherited from the Heidelberg-Moscow experiment, can create larger detectors, allowing for more exposure for the same number of support structures, cables, etc. that may introduce radioactive backgrounds. The p+ point contact (PPC) and broad energy germanium (BEGe) geometries, used in the MAJORANA DEMONSTRATOR and GERDA respectively, have much smaller p+ contacts, decreasing the detector capacitance, reducing noise, and improving pulse shape discrimination performance. The inverse coaxial point contact (ICPC) geometry is an innovation of the LEGEND collaboration that combines the excellent energy resolution and pulse shape discrimination performance of PPC and BEGe detectors with the increased mass of coaxial detectors [29]. LEGEND-1000 will transition to using ICPC detectors exclusively, so understanding the response of these detectors to different types of incident radiation is crucial for understanding the backgrounds in LEGEND-1000.

While the weighting potential itself is only dependent on geometry, the $\Delta\phi$ quantity in Eq. 2.1 is also dependent on the drift path of the electrons and holes. These are dependent on both the detector geometry and the impurity profile of the germanium, which shape the internal electric field. Neither of these quantities

are particularly well-documented by detector manufacturers, creating uncertainties in simulations of detector signals. Attempts to address these uncertainties are described in Ch. 4.4.2.

2.2 Background Sources

Radioactive backgrounds in LEGEND predominantly originate from the ^{238}U and ^{232}Th decay chains, which supply a number of γ lines, βs, and αs. An additional source of α contamination comes from ^{220}Rn, which is found in the atmosphere. Any contamination, especially of the passivated surface, can lead to α particles emitted directly into the active volume of the detector, bypassing the LAr veto. Surface effects also cause these events to become energy degraded, so while they are emitted at $5 - 7$ MeV, they can be reconstructed with much lower energies and end up in the ROI near $Q_{\beta\beta}$. Thus, detectors need to be kept under vacuum or in clean nitrogen atmospheres at all times.

The liquid argon itself, while a crucial component of LEGEND's background mitigation strategy, also introduces background contamination in the form of the cosmogenically activated isotope ^{42}Ar. ^{42}Ar decays into ^{42}K, which in turns β decays, emitting a β with an endpoint energy of 3.5 MeV. These ^{42}K ions can drift within the LAr, attracting to the high voltage detector surfaces. They can then, similar to radon, decay on the detector surface, emitting a β that bypasses the LAr veto and becomes energy degraded.

Surface events such as αs and ^{42}K βs make up the largest components of the projected LEGEND-1000 background budget, shown in Fig. 2.5. This effect will be mitigated by the use of LAr sourced from underground, where there is less naturally activated ^{42}Ar, and backup technologies such as PEN encapsulation are being investigated to minimize the volume of LAr that is exposed to the detector surface. Meanwhile, improving PSD techniques to identify and remove surface backgrounds will be crucial to meet LEGEND-1000's background goals.

2.3 Pulse Shape Discrimination

To eliminate background radiation, there are two main features of $0\nu\beta\beta$ decay events that our pulse shape parameters attempt to capture. First, the $0\nu\beta\beta$ decay is a *single-site event* (SSE). The emitted electrons deposit their energy in $\mathcal{O}(1\text{mm})$ around the decay site. This can be contrasted with gamma events that often

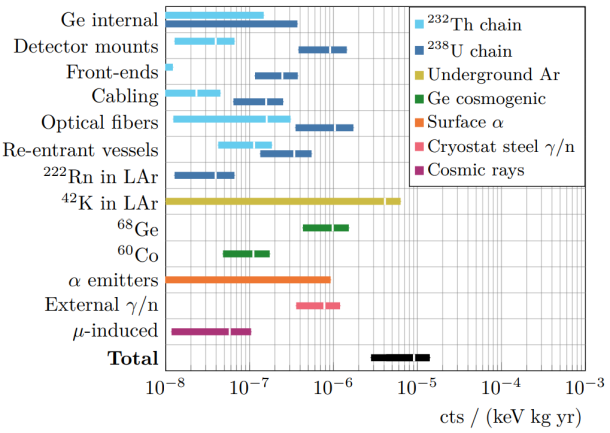

Figure 2.5: Projected significant backgrounds in LEGEND-1000 [30].

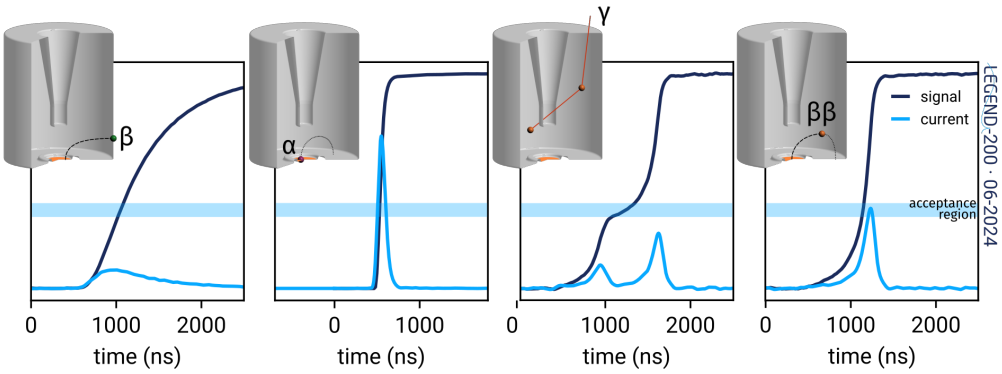

Figure 2.6: Different events have characteristic pulse shapes that allow us to distinguish signal-like and background events. From left to right, we have a surface β entering the n+ contact, a surface α entering the passivated surface, a multi-site γ, and $0\nu\beta\beta$-like, single-site, bulk event. The waveforms are shown in dark blue, while their derivatives are shown in light blue.

Compton scatter and have multiple interaction points separated by $\mathcal{O}(1\text{cm})$. These types of events are called *multi-site events* (MSEs). Their waveforms are distinguished by a "step" in the rising edge, shown in Figure 2.6.

The second defining characteristic of $0\nu\beta\beta$ decay events is that they are more likely to originate from the *bulk* of the detector than the detector *surface*. External radiation, such as betas and alphas, often cannot penetrate very deep into the detector, so rejecting surface events allows us to create a fiducialized volume of germanium that is self-shielding. $0\nu\beta\beta$ decays could, of course, occur in the ^{76}Ge atoms near the detector surface, but these events often have incorrectly reconstructed energies due to effects such as incomplete charge collection in the dead layer created by the n+ contact and charge trapping near the passivated surface.

This means that signal events are unlikely to be correctly categorized, and background events are likely to be incorrectly categorized near the surface. Thankfully, surface events also exhibit pulse shape features that allow us to distinguish them from bulk events. As shown in Figure 2.6, surface events often have either very fast or very slow rise times, slower rollover in the top corner, and positively sloping tails.

2.3.1 Cut Calibration

The analysis chain to perform pulse shape discrimination is focused on quantifying these differences and setting cuts to improve background rejection while preserving signal. This requires a set of events that can behave as proxies for a $0\nu\beta\beta$ decay event. One option is the $2\nu\beta\beta$ decay spectrum, which is topologically identical to the $0\nu\beta\beta$ signal, but by definition occurs at energies lower than $Q_{\beta\beta}$ and with low statistics. Another option is the double escape peak (DEP) from a γ line. This is a population of events created from an incoming gamma of energy E_0 that interacts with a germanium atom through pair production, creating an electron and a positron with a combined mass and kinetic energy of E_0. The electron deposits its kinetic energy, creating electron-hole pairs, until it thermalizes with lattice electrons. The positron deposits its kinetic energy until it annihilates with an electron in the lattice, creating two back-to-back 511 keV γs that can escape from the edges of the detector. This creates a bulk event consisting of two βs depositing their energy in a single site with energy $E_0 - (2 \times 511)$ keV.

In addition to their energy distributions, another key difference in the DEP and $2\nu\beta\beta$ populations is their distribution within the detector. Because the DEP event requires both gammas, produced back-to-back, to escape the detector, they are more likely to occur in the "corners" of the detector. The $2\nu\beta\beta$ events should be isotropically distributed within the detector, exactly as $0\nu\beta\beta$ events.

LEGEND-200 performs weekly calibration runs with a ^{208}Tl source. The 2615 keV gamma from this source creates a DEP at 1593 keV, giving us a high statistics $0\nu\beta\beta$ proxy, with a trade-off that it is not very near $Q_{\beta\beta}$. This population is used to investigate drift time and energy dependence and evaluate survival fraction of $0\nu\beta\beta$-like events.

Parameters are calibrated across *partitions* of stable detector performance to remove dependencies on energy, time, and drift time. Cut thresholds are typically set in order to establish a 90% survival fraction of DEP events. The digital signal processing (DSP) filters, calibration routines, and automated processing are

handled through LEGEND' custom software framework, `pygama` [31].

2.3.2 Rising Edge Parameters

To capture differences in the rising edge of the waveform, we look at the maximum of the first derivative. According to Eq. 2.1, the signal rises the fastest when the electron-hole pairs drift through regions of steeply varying weighting potential. These regions are located close to the point contact. Thus, for n+ surface events, the maximum value of the derivative will be smaller than that of signal-like events. For alphas entering the passivated surface, the derivative will be larger. For MSEs, the step along the rising edge results in a smaller maximum derivative.

The derivative can be calculated in different ways. In the LEGEND-200 analysis chain, it is calculated as a moving window average and the maximum of this value is called A, for current. This value is then normalized by the height of the waveform, i.e. the event energy, E. The energy is calculated as the maximum of a truncated cusp filter. The final parameter used for cuts is then A/E.

The derivative can also be calculated as the maximum of a triangle filter, T, which also gets normalized by energy becoming T/E. This is the parameter used in the analysis of test stand data from CAGE, discussed in Ch. 3.

2.3.3 The Late Charge Parameter

The late charge (LQ) parameter, visualized in Figure 2.7, was developed in order to discriminate alpha events. It captures the slow roll-over in the upper corner of the waveform, a shape unique to alphas entering through the passivated surface. This is caused by charge trapping along the surface, where charges along the insulating surface and defects in the crystal lattice capture drifting charges and re-release them on the timescale of the signal collection. This causes a portion of the electron-hole pairs to be collected later in the waveform.

It is calculated by integrating the flat top of the waveform, and subtracting the integral of the waveform after the the waveform reaches 80% of its maximum (`tp_80`) through the use of a trapezoidal filter. This effectively gives the area of the waveform above `tp_80`, which will be higher for alpha events than bulk events. This value is also normalized by the event energy.

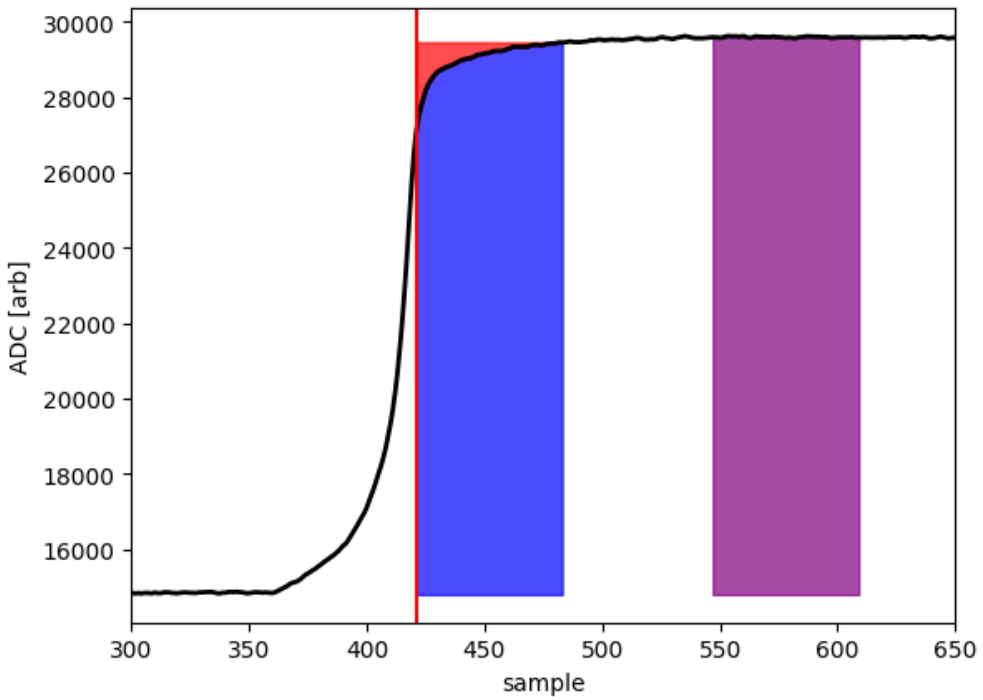

Figure 2.7: Calculation of the LQ parameter. The blue integration window is subtracted from the purple integration window, leaving the area in red, which becomes the raw `lq80` parameter.

Chapter 3

The CAGE Scanner

The Collimated Alphas, Gammas, and Electrons (CAGE) scanner was designed to study surface events in a variety of germanium detector geometries. To date, the test stand has housed and scanned two different germanium detectors, focusing on the study of alpha radiation entering the active volume through the passivated surface. In this chapter, I will describe the hardware modifications I have made to accommodate scans of a larger detector and improvements to the precision and stability of the scanner.

3.1 Hardware Overview

CAGE consists of a vacuum cryostat atop a liquid nitrogen dewar that provides cooling. A copper cold finger extends out of the dewar and connects to a copper cold plate, where the detector is installed. The detector setup is surrounded by a copper "top hat" that acts as an IR shield to minimize leakage current. A lead collimator with an ^{241}Am source is installed internal to the top hat, which can be lifted and moved, allowing a collimated beam of alphas to be directed at specific points of the detector surface. This source is situated on a system of three motors, shown in Fig. 3.1, a rotary motor, which controls the polar angle of the source beam, a linear motor, which controls the radial position of the source beam, and a source motor, which controls the incidence angle between the source beam and detector surface.

On top of the cold plate lies a sapphire disk, that is electrically insulating but thermally conductive, and a copper HV ring. The germanium detector sits, with the p+ contact pointed up, on top of the HV ring. The front end electronics are supported by a ring and diving board made of PEEK, a plastic that is insulating and

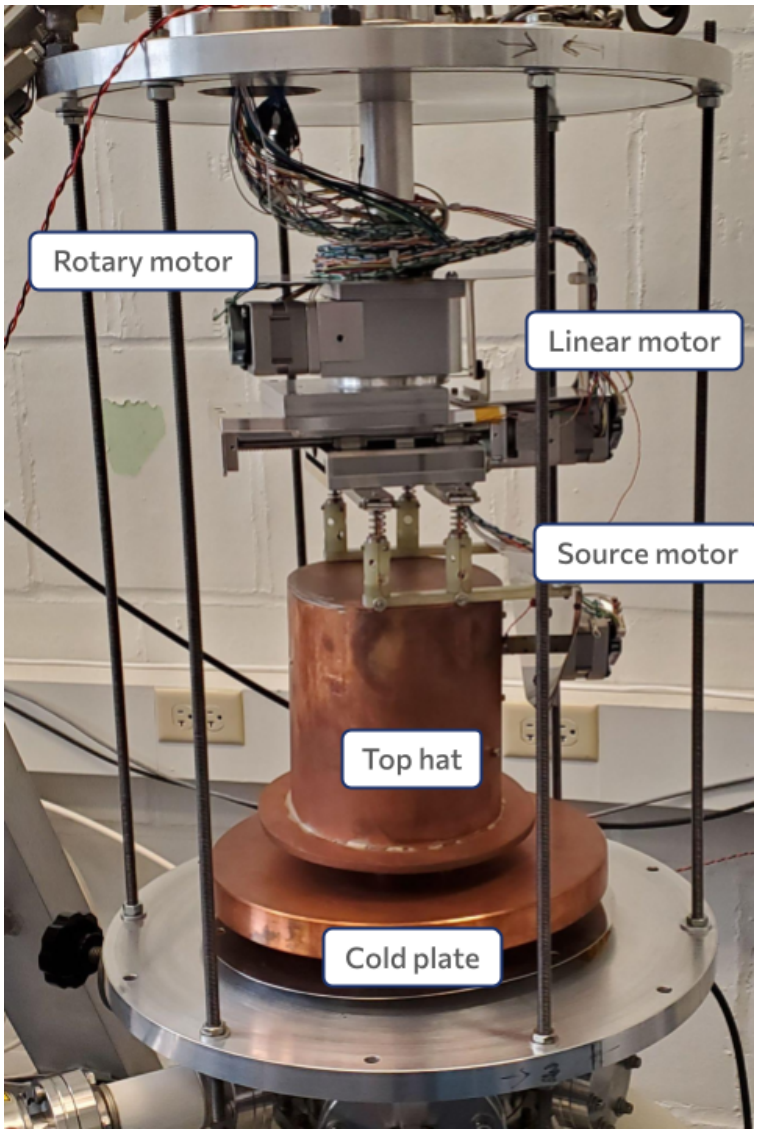

Figure 3.1: The CAGE scanner, with major components labeled. It is installed in the "CAGE cage" alignment stand described in Section 3.2.3. The rotary motor selects the polar angle along the detector surface for source movement and the linear motor controls the radial position of the source. The source motor allows the source beam to rotate and hit the detector surface at varying incidence angle.

Figure 3.2: Comparison of PEEK support structures for detector and front end electronics board for OPPI *(left)* and ICPC *(right)*.

outgasses minimally. The front end board makes contact with the p+ contact of the detector through a pogo pin. This configuration is shown in Fig. 3.2.

3.2 Modifications

3.2.1 ICPC Accommodations

In its initial data taking campaigns, CAGE was used to scan and characterize OPPI, a prototype PPC geometry detector. The results of those scans can be found in [32]. To better serve the next generation of the experiment, we aimed to perform similar scans for the ICPC geometry detectors that will be deployed in LEGEND-1000. To do so required hardware modifications for the larger detector. First, the taller detector required longer aluminum posts to hold the PEEK ring that centers the detector, as well as G-10 sheaths around the posts to mitigate the chance of sparking between the high voltage n+ contact and the posts. New holes were drilled in the top hat IR shield to lift the source collimator and maintain the same distance between source and detector surface. Finally, the larger radius of the detector necessitated a redesign of the holder for the front end electronics. The original diving board design could not exert enough downwards force to maintain good contact between the pogo pin and p+ contact when adapted to the larger detector radius. Instead, the diving board was extended into a "bridge" that extends across the entire diameter of the

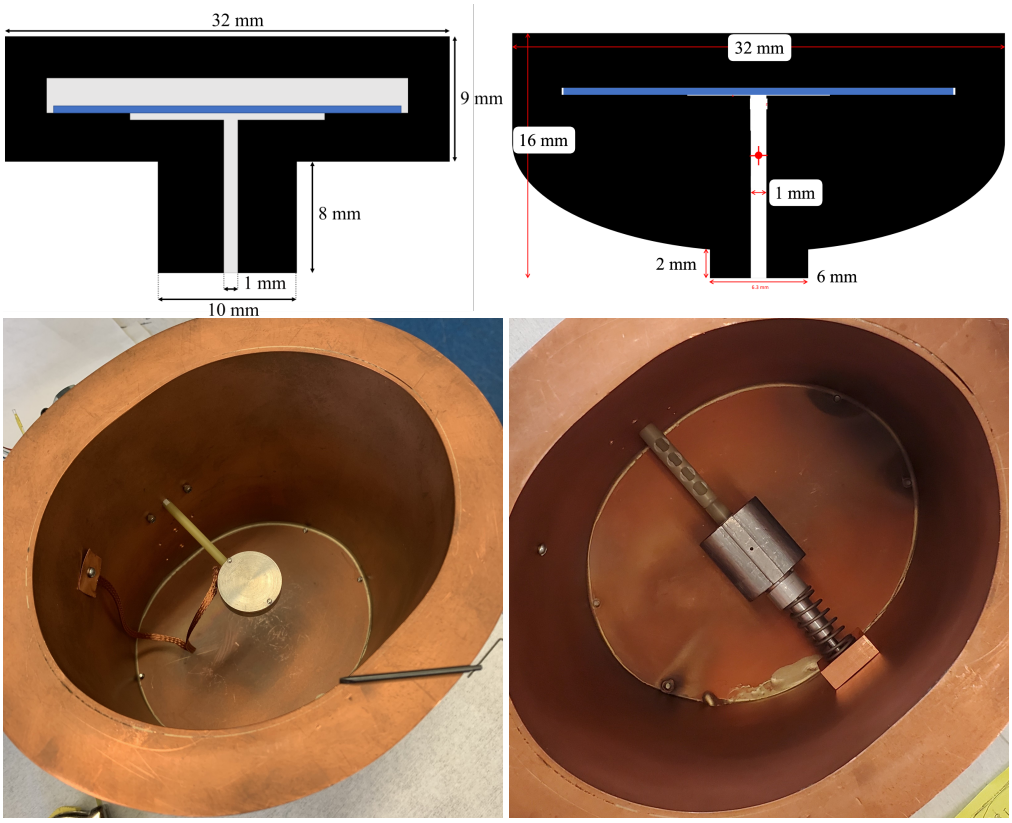

Figure 3.3: *(left)* Original collimator design and *(right)* redesigned collimator with aluminum crossbar. Cross sectional drawings of the lead source holders are shown in the top images.

detector. While the diving board itself has a width of 7.2 mm to accommodate the front end, the extension is made with a thinner width of 3.1mm to maximize the amount of detector surface that remains exposed while providing enough support to ensure good contact. In addition, a PEEK cap is placed on top of the front end electronics and secured to the bridge with nylon screws to prevent upwards force on the pogo pin from displacing the electronics board. These modifications are shown in Figure 3.2.

3.2.2 Collimator Design

The collimator was originally designed to sit at the end of a G-10 insulating shaft connected to the source motor, cooled by a copper braid connecting the lead collimator to the interior of the top hat. This design had two main flaws. The first being that supporting the collimator on only one side introduces position uncertainty in the form of an extra degree of freedom in the angle that the shaft makes from horizontal. The second being that screwing the copper braid into the soft lead collimator was unreliable and often found

to have loosened over the course of multiple thermal cycles and motor movements, risking loose hardware falling and damaging the detector.

Our redesigned collimator, shown in Figure 3.3, alleviates both of these issues by supporting the other side of the collimator with a metal shaft that is directly screwed into the top hat, fixing the shaft angle. At the end of the metal shaft, a copper block is pressed into the top hat with a spring, providing thermal contact. Care was taken to safely reach incident angles of 45° from normal by curving the edges of the collimator and maintaining the distance between source and detector surface to ensure the continued validity of our simulations.

3.2.3 Improved Alignment

In order to better understand the position uncertainty of our beam, we constructed the "CAGE cage," an in-air stand that mimics the installation of the top hat inside the cryostat, but allows us to make measurements of the top hat position relative to the cold plate. This stand consists of threaded rods placed in the bolt holes used to secure the flange to the cryostat body, with the flange held at the correct height with nuts and washers threaded onto each rod. Measurements of the top hat position on the cold plate at each of our rotary scan angles, 0°, 145°, and 180°, were made as well as measurements of the linear motor position. We found a number of misalignments in the system, creating a multiple millimeter uncertainty in our previous beam positions.

First, we found that the cold finger supporting the cold plate has a 0.6° tilt from vertical, creating a 3.75mm discrepancy between the center of the cold plate and the center of the cryostat. The cause is suspected to be uneven placement of indium chips at the base of the cold finger, used to improve thermal conductivity between the cold plate and liquid nitrogen dewar. This should not affect the beam position relative to the detector, but it does affect our ability to modify the cold finger in the future without making adjustments to our motor positioning.

Second, the rotation axis of the top hat was found to be 4mm away from the center of the cold plate, creating an up to 9mm offset in the expected beam position, depending on rotary angle. After re-machining the alignment plates of the rotation axis, the distance between the center of cold plate and center of rotation axis was brought to 0.96 ± 0.18mm. This is then used to calculate the motor positions that will bring the

beam to the expected location on the detector surface.

3.3 First ICPC Scans

3.3.1 Datataking

In the first datataking campaign with the ICPC detector, we aimed to scan the passivated surface, which extends between the p+ dimple and the outer edge of the ditch, at three different rotary angles and normal beam incidence. This is accomplished by performing a linear scan at one rotary angle at a time. The rotary limit switch is pressed to establish a rotary angle of $0°$. Then, the linear motor is moved forward 2.5mm from its limit switch to center the source on the detector surface, establishing a linear position of 0mm. A *run* is defined as a continuous datataking period ($\mathcal{O}(10)$ minutes to $\mathcal{O}(10)$ hours) at a single source position, which is split into individual *cycle* files of 10-30 minutes each. After each run, the linear motor is then driven forward $1-2$mm to the next source position. After taking data at the desired linear positions, the linear motor is reset to the center of the detector, and the top hat is rotated to the next rotary angle. For *background* runs, the source points up, away from the detector, and the source is rotated $180°$ to normal incidence with the detector surface for *alpha* runs. A *dataset* is the background and alpha data taken at all rotary and linear positions in a single cooldown.

The front end electronics and post-amplifier are made in-house at CENPA following the MAJORANA design [33]. After the second-stage amplification, the signal is collected by a Struck SIS3302 16-bit digitizer at 100 MHz sampling rate. The data collection is controlled with ORCA [34] and processed with a custom fork of the `pygama` processing chain on the NERSC computing cluster.

Slow controls data, including temperature sensors on the top hat and cold plate, the pressure gauge, detector baseline, and bias voltage are monitored by a Raspberry Pi running `dragonfly`, the slow controls monitoring tool developed by Project 8 [35]. The slow controls data is stored in a PostgreSQL database, which can be accessed offline for more in-depth analysis, as well as viewed in real time with a SlowDash [36] dashboard. A software interlock will trigger an automatic bias down of the detector in the event of a hardware failure that causes large deviations from the expected values of temperature, pressure, or baseline. A demonstration of the stability of slow controls data for each of the datasets analyzed in this chapter is

shown in Fig. 3.4.

3.3.2 Data Processing

Data is taken as binary files which are transferred to and stored on the NERSC computing cluster. There, our custom software, `autogen`, based on a fork of LEGEND's `pygama` analysis stack, is used to process data through three stages. First, the `raw` stage decodes the binary file and contains the waveform signal, digitizer energy estimate, and metadata from the digitizer. Then, the `dsp` tier calculates our uncalibrated waveform parameters, including energy and parameters used for pulse shape discrimination. Finally, the `hit` tier uses the DSP parameters for a full run in aggregate to calibrate parameters and set cuts.

3.3.3 Detector Characterization

Detector Depletion and Bias

The depletion voltage and recommended operating voltage for a detector is generally characterized by the detector manufacturer and provided on its datasheet. This information, however, was not provided for the ICPC operated in CAGE. Instead, we verify that the detector is giving signals consistent with depletion by measuring the rise times of signals as we apply higher bias voltages. When the detector depletes, regions of poor charge mobility within the detector disappear, and the waveforms "sharpen" with noticeably shorter rise times. This was observed by eye on an oscilloscope multiple times, and measurements of the rise time on oscilloscope signals were taken twice, shown in Fig. 3.5. Measurement 1 (2) was taken as the average of 2 (3) waveforms per bias voltage, measuring the rise time of the signals using the oscilloscope cursors. From these observations, the depletion voltage was found to be approximately 2900 V. Detectors are typically operated at an additional 500 V over depletion to account for any changes in depletion voltage that may occur over time and minimize regions of incomplete charge collection. This must be balanced with an increase in leakage current as the detector is pushed closer to its breakdown voltage.

As discussed in Sec. 4.4.2, measurements of ICPC's CV curve, taken after the scans shown in this work, hint that the detector may not be fully depleted, even at 3500 V. The combination of fast signals and an unstable capacitance measurement implies that there may be "pinch-off" occurring, a phenomenon where the depleted region reaches both contacts but leaves an undepleted bubble in the center.

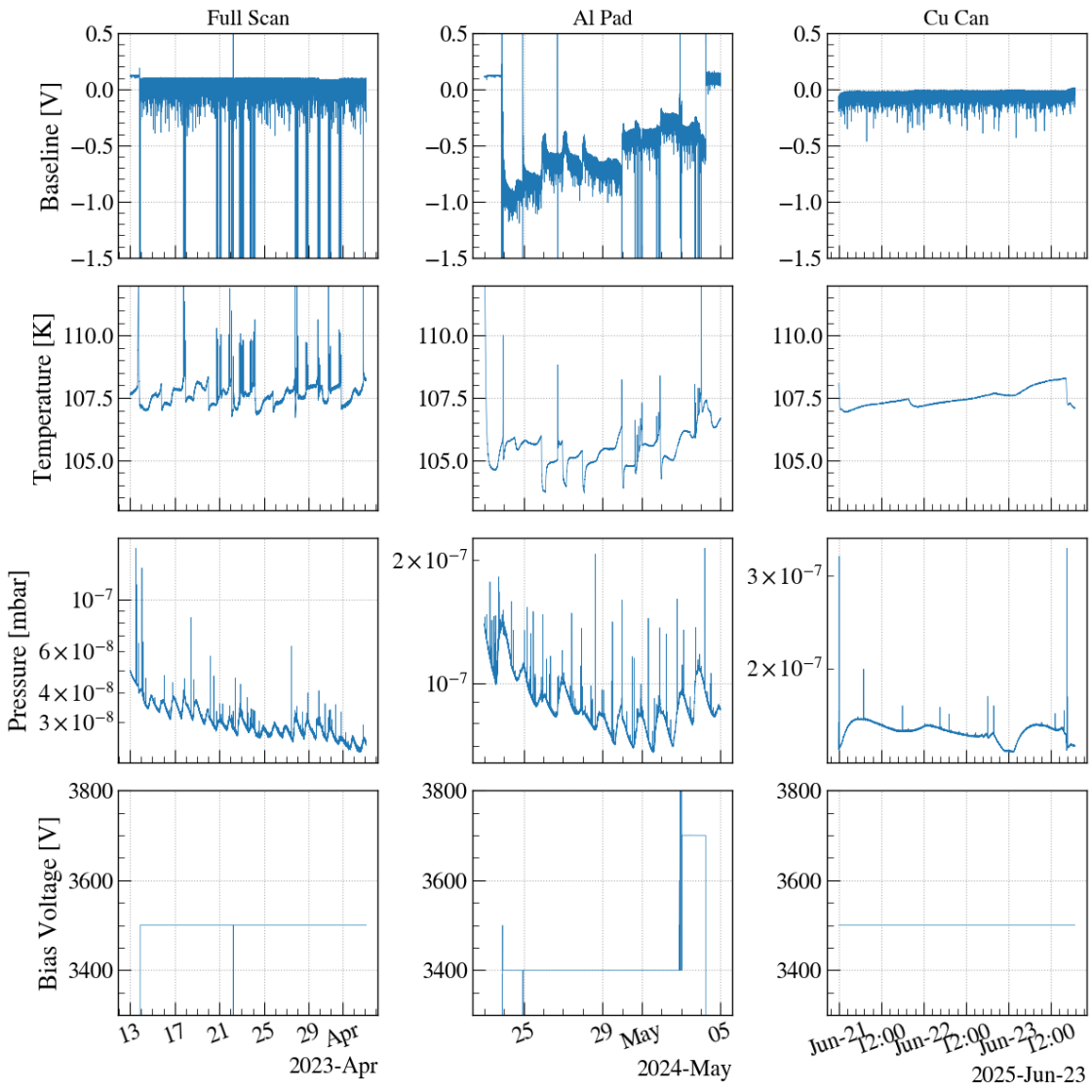

Figure 3.4: Demonstration of stability of slow controls data over a run at a single scan position for each of the major datasets shown in this chapter. Large spikes in the baseline correspond to movements of the source and changes in bias voltage. Spikes in the pressure reading are attributed to artifacts of the gauge readout.

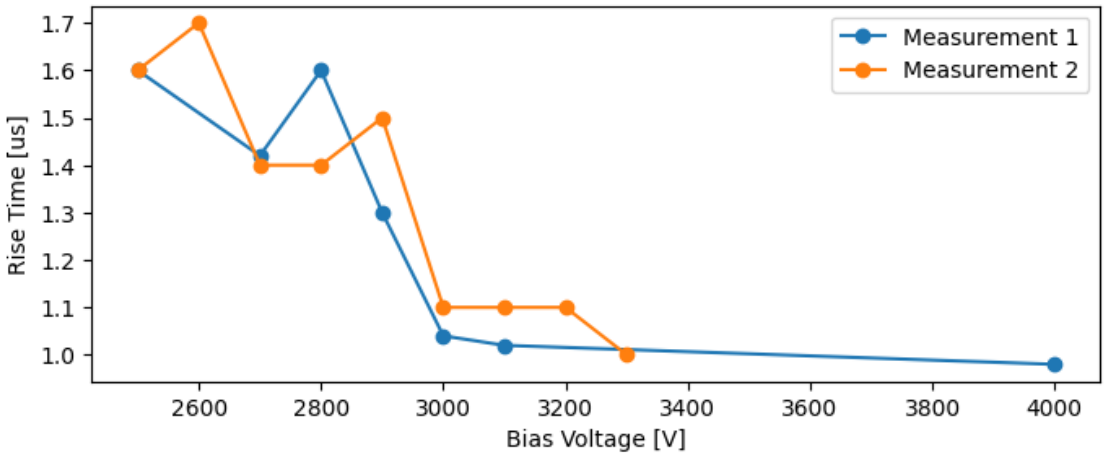

Figure 3.5: Rise time vs. bias voltage for physics signals in ICPC. The drop in rise time between 2800 V and 3000 V corresponds to depletion of the detector.

Energy Resolution and Linearity

As discussed in Section 1.4.2, energy resolution is one of the major considerations in choosing a technology for $0\nu\beta\beta$ decay searches. We use the maximum of a trapezoid filter as an energy estimator, `trapEmax`. This is then calibrated using a scaling factor.

$$E_{cal} = cE_{raw} \tag{3.1}$$

where c is determined by the most prominent peak in our data, the 1460 keV gamma line from ^{40}K. We then characterize the linearity and resolution of our detector by fitting expected peaks in a range of energies from common radioactive backgrounds in our surface lab, shown in Table 3.1. The peaks are fitted to a Gaussian with an exponential decay low-energy tail, on top of a linear step background. The Gaussian μ and σ are taken from this fit to calculate the peak position and FWHM, shown in Fig. 3.6. The peak residuals demonstrate a small remaining quadratic component to the calibration, but as none of our analysis depends heavily on precise energy estimation, we continue to operate with a one-point linear calibration.

Detector Dimensions

In addition to understanding the alignment of our motor system, we also need to understand the geometry of the detector to ensure our beam is pointing accurately to detector features. Unfortunately, the datasheet

Source	Energy [keV]
β^+	511.0
^{228}Ac	911.2
^{40}K	1460.8
^{214}Bi	1764.5
^{208}Tl	2614.5

Table 3.1: List of background γ peaks used to characterize detector linearity and resolution

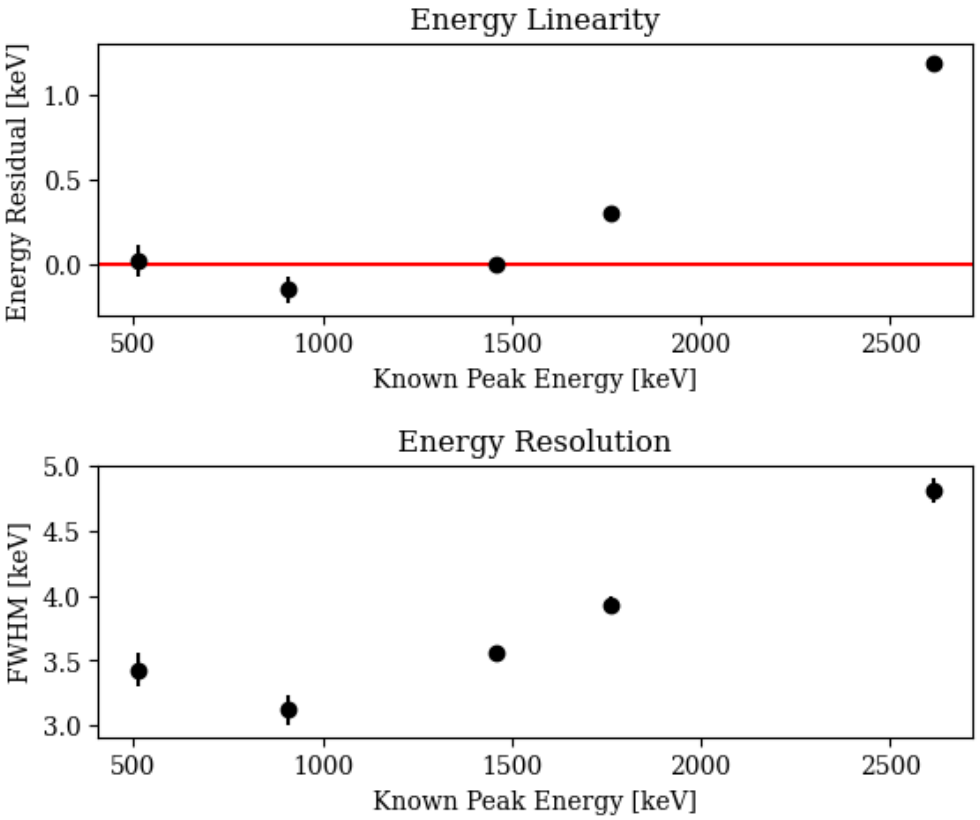

Figure 3.6: *(top)* $E_{cal} - E_{true}$ for each peak in a background run. Calibration is determined by the ^{40}K peak, fixing its residual near 0. *(bottom)* FWHM for each known peak, translating to an energy resolution of 0.2% at 2615 keV.

provided by the manufacturer is missing key geometric information, such as the dimensions of the bore hole and passivated ditch. Measuring these features with traditional rulers, especially the passivated surfaces, is not feasible due to the sensitivity of these surfaces to scratches that would alter detector behavior. Instead, we measured our detector dimensions at the University of Washington's X-ray Computed Tomography Facility with an NSI X5000 CT scanner [37]. This gave us an image of the cross section of our ICPC detector, shown in Fig. 3.7. We then counted the pixels in this image corresponding to each feature and converted to physical measurements using the manufacturer provided detector height and width, giving us dimensions with an uncertainty of 0.5 mm on our measurements.

The bore hole, approximated with a trapezoidal cross section, has a larger diameter of 30.4 mm on the bottom of the detector, and a smaller diameter of 8.8 mm at a depth of 57.2 mm into the detector center. Since the CT scanner image does not clearly delineate the border between bore hole and germanium, this depth was measured with calipers. The n+ contact covering the bore hole can be touched, unlike the p+ contact and passivated surface. The bore hole dimensions are not used in analyzing CAGE scan data, but they are used as an input in the simulations discussed in Sec. 4.4.2. The dimensions relevant to the CAGE scans are the point contact and especially passivated ditch dimensions.

The point contact dimple dimensions are given by the manufacturer as 5.7 mm at its widest point, with a depth of 2.1 mm. Our measurements returned a diameter of 5.4 mm and a depth of 2 mm, giving confidence in our method. As our ICPC was manufactured by ORTEC, the p+ contact is fully situated within this dimple. This is contrasted with Mirion manufactured ICPCs, where the p+ contact extends until the passivated ditch. We measured the passivated ditch to have an inner radius of 14.1mm, an outer radius of 19 mm, and a depth of 1.7mm. Interestingly, the bottom of the ditch is rounded, rather than coming to right angles as previously thought. The data shown in this thesis was taken prior to making these measurements of the detector. That means our furthest linear scan positions only go to 14mm, probing the passivated ditch, but not fully covering it.

We will also need to know the dimensions of the front end bridge that lays across the detector surface. The alphas and gammas emitted by ^{241}Am are unable to penetrate the PEEK material and front end board, so we do not expect to see americium events until the beam is driven past the edge of the bridge. From caliper measurements of the board, and measurements of the alignment angle performed with the CAGE cage

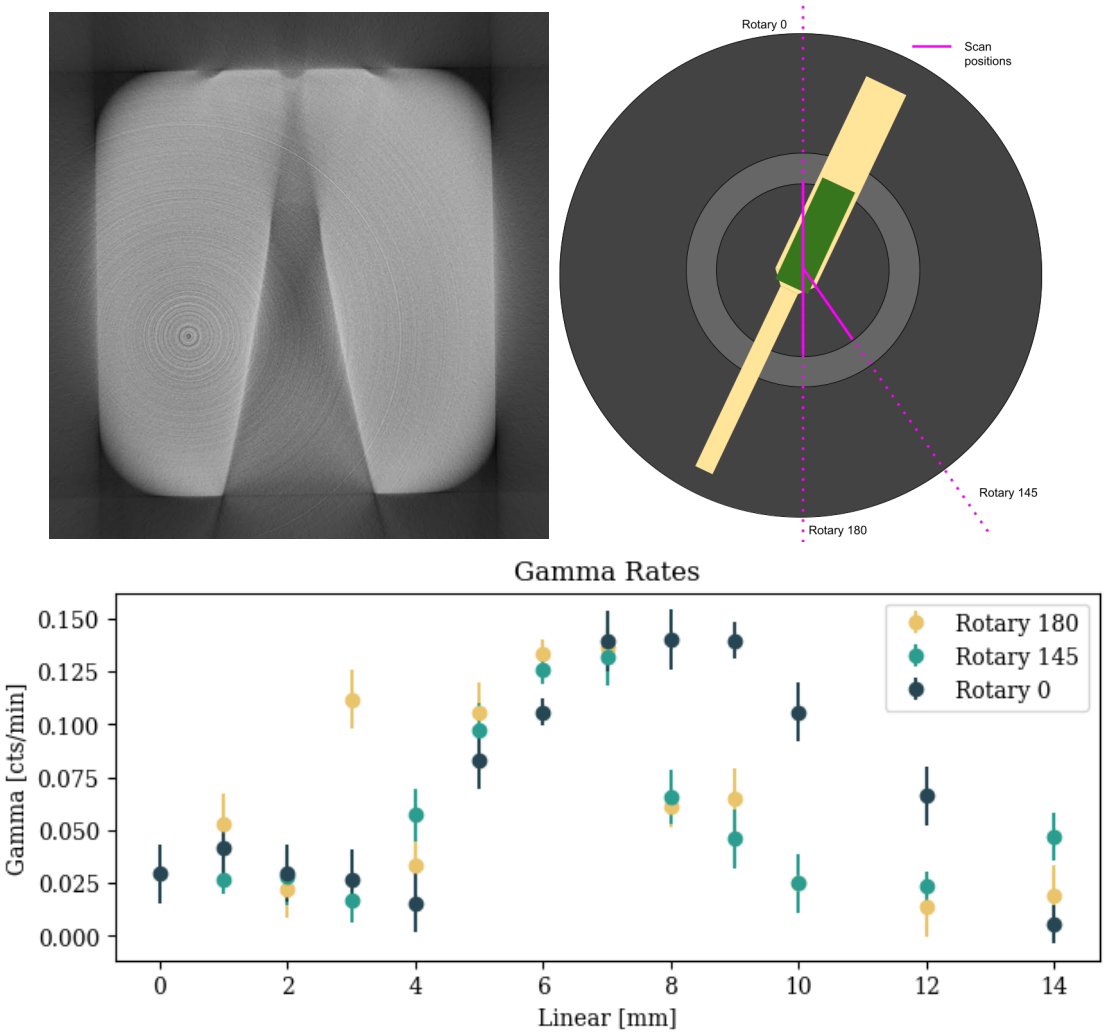

Figure 3.7: *(top left)* The CT scan image of the ICPC detector which was used to determine dimensions. *(top right)* Schematic of the top view of ICPC with rotary positions shown in dotted pink lines and the extent of the linear scans shown in solid pink lines. *(bottom)* Rate of 60 keV gamma events by scan position, which rises between 3 and 4 mm as expected from measurements of the front end holder.

described in Section 3.2, we find the distance from the center of the detector to the edge of the front end bridge is 4.4 mm, 4.1 mm, and 4.4 mm for rotary angles $0, 145$, and 180 respectively. Previous simulations of the system demonstrated a spot size of 2mm in diameter [32], which our collimator modifications were careful to maintain. This means that we should expect to start seeing americium events at linear positions of $3 - 3.5$mm at each rotary position, and that is consistent with what we see in our measurement of the 60 keV γ peak, shown in Fig. 3.7.

3.4 Alpha Identification

CAGE is designed to study surface events and develop PSD techniques to identify and remove them. Our current ^{241}Am source provides surface alphas and shallowly impinging 60 keV gammas. In this section, we will focus on identifying alpha events.

First, we measure the total alpha rate by performing a background subtraction on the calibrated energy spectrum. The energy spectrum for a background run, normalized by runtime, is subtracted from the runtime-normalized energy spectrum for an alpha run at a given position. The alpha rate is then determined by summing the remaining counts above an energy threshold of 1000 keV, excluding a ± 10 keV range around the prominent gamma peaks at 1460 and 2615 keV. These spectra and rates for each scan position are shown in Figure 3.8.

We will compare the alpha identification performance and overall trends of two PSD parameters that were used in scans of the OPPI detector with CAGE, DCR and T/E.

3.4.1 Delayed Charge Recovery

Delayed charge recovery (DCR) is a parameter that was used in the MAJORANA Demonstrator for alpha identification [38]. It relies on the physical phenomenon of charge trapping, the same process that is exploited in the use of of the LQ parameter (see Sec. 2.3). DCR, however, focuses on the tail of the waveform rather than the upper corner. After the waveform is pole-zero corrected, a $0\nu\beta\beta$-like event will have a flat tail. Due to the late charge collection in events effected by surface trapping, this tail will instead have a small upwards slope. DCR is a measure of this slope.

It is calculated with a trapezoidal filter, with a long flat time of 20 μs and a rise time of 7 μs. The DCR

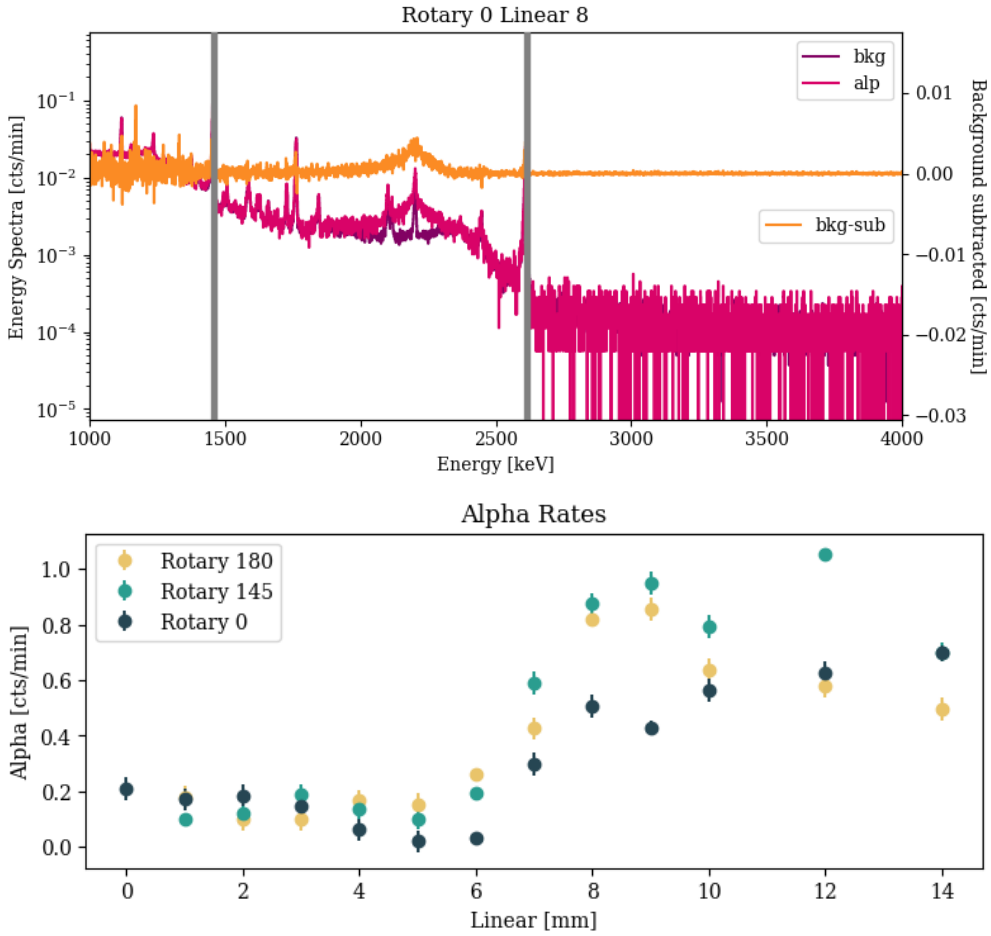

Figure 3.8: The top image shows an example of background subtraction for one linear scan position. The purple and pink spectra of the runtime-normalized background and alpha runs, respectively, are shown on a log scale. The background subtracted spectrum is shown in orange. This spectrum is summed over all bins above 1000 keV, except the bins around known gamma peaks represented by grey bars, to get the alpha rates shown in the bottom plot.

parameter is then picked off of this trapezoid at a fixed time of 80 μs. This is an effective average slope of the pole-zero corrected tail between $60 - 80$ μs.

The alpha populations in our ICPC scans can be seen in DCR on the right side plots of Fig. 3.10-3.12. These show DCR vs. energy at selected radial positions, 3mm, 7mm, 10mm, and 14mm. At 3mm, the source beam has not yet cleared the PEEK front end bridge, so no alphas are expected. The beam at 14mm is lying inside the passivated ditch.

We expect the value of DCR for surface alphas to be higher than for bulk events. In previous scans of the OPPI PPC-style detector, DCR was found to be high for alpha events near the point contact and decreased with increasing linear position until they sink into the bulk distribution [32].

In our ICPC scans, DCR followed this same trend at rotary 145° and 180°, but at rotary 0, the alpha distribution is very spread out in DCR and is still very visible at a radius of 14mm. This suggests a rotational asymmetry, which would be unexpected. Repeated scans after rotating the detector 180°, would shine light on the nature of this asymmetry.

3.4.2 T/E

T/E, as discussed in Section 2.3, is a measure of how quickly the waveform rises to its maximum amplitude. It is calculated on CAGE data with a triangle filter on a pole-zero corrected waveform. The rise time of the filter is 10 samples and the flat time is 1 sample. This is the normalized by an energy estimator, `trapEmax`, the maximum of a trapezoidal filter with rise and flat times optimized to get the best energy resolution of the 1460 keV peak. This value is then calibrated to account for drifting of T/E between runs, as shown in Figure 3.9. At each scan position, the central value of the T/E distribution, $\mu_{T/E}$, is found, and a `cal_ToE` value is calculated as

$$\texttt{cal\_ToE} = \frac{\text{T/E}}{\mu_{T/E}} - 1 \tag{3.2}$$

This drifting of T/E is reminescent of A/E instability in ORTEC-manufactured ICPC detectors installed in LEGEND-200, also shown in Fig. 3.9. While there may be other systematics, such as pinch-off discussed in Sec. 3.3.3 or top hat motion explored in Sec. 3.5.2, at play, this points towards differences in the manufacturing process between the two detector manufacturers, Mirion and ORTEC. The largest difference in the two manufacturers is the geometry of the point contact, with Mirion detectors having wider, disk-like

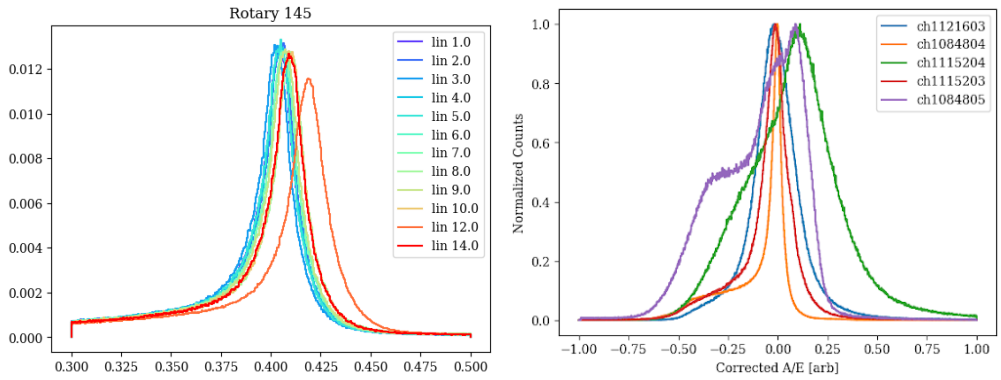

Figure 3.9: *(left)* The central value of the uncalibrated T/E distribution measured in the CAGE ICPC drifts between runs, and occassionally experiences large jumps. *(right)* A similar instability is also observed in A/E for ICPC detectors manufactured by ORTEC installed in the LEGEND-200 array.

p+ contacts that extend to the passivated ditch and ORTEC detectors having p+ contacts that only fill the central dimple. This results in a larger passivated surface area that is sensitive to charge buildup which can impact the internal electric fields and charge collection.

We expect surface alphas to have high values of T/E. The passivated surface is relatively close to the p+ contact, where there is the largest change in weighting potential. This corresponds to a large immediate contribution to the waveform signal, according to Eq. 2.1. Alpha populations are visible in T/E in the left side plots of Fig. 3.10-3.12.

As for DCR, the behavior observed in OPPI was a high value of T/E near the point contact that gradually decreases as the linear motor is driven out radially. In our ICPC scans, we find that this trend has inverted, with alpha events becoming better separated at larger linear positions.

These complementary trends between T/E and DCR should allow us to use a combination of both parameters to effectively identify alphas at all radial positions, rather than just close to the point contact, as was the case in the OPPI detector.

3.5 Exploratory Hardware Improvements

3.5.1 HV Connection

The original CAGE design applied high voltage to the n+ contact using a copper HV ring that the detector sat upon. We found that the room temperature resistance between the front end board and the ring was a

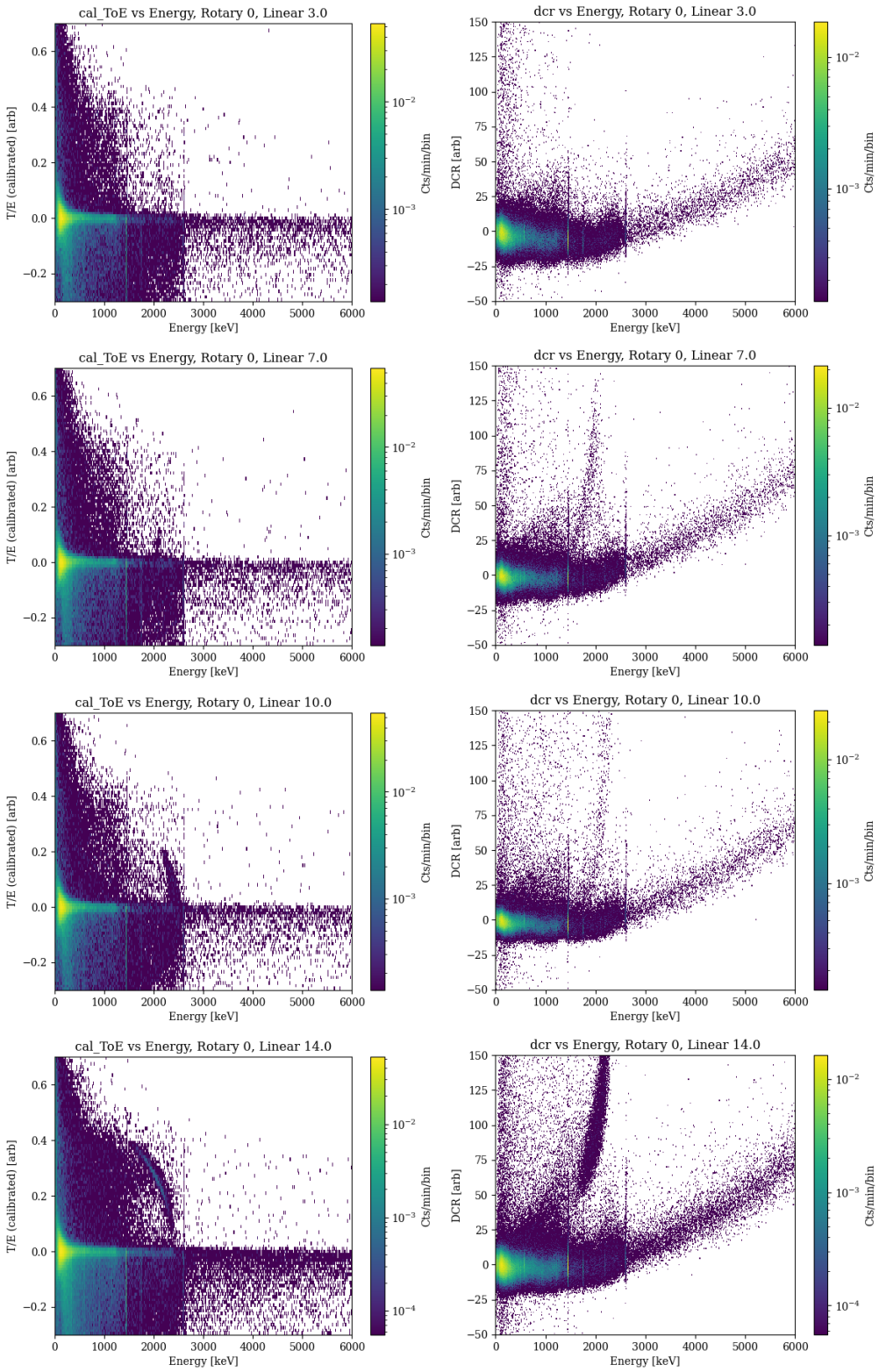

Figure 3.10: T/E *(left)* and DCR *(right)* vs. energy for rotary 0, linear 3, 7, 10, 14 mm scan positions.

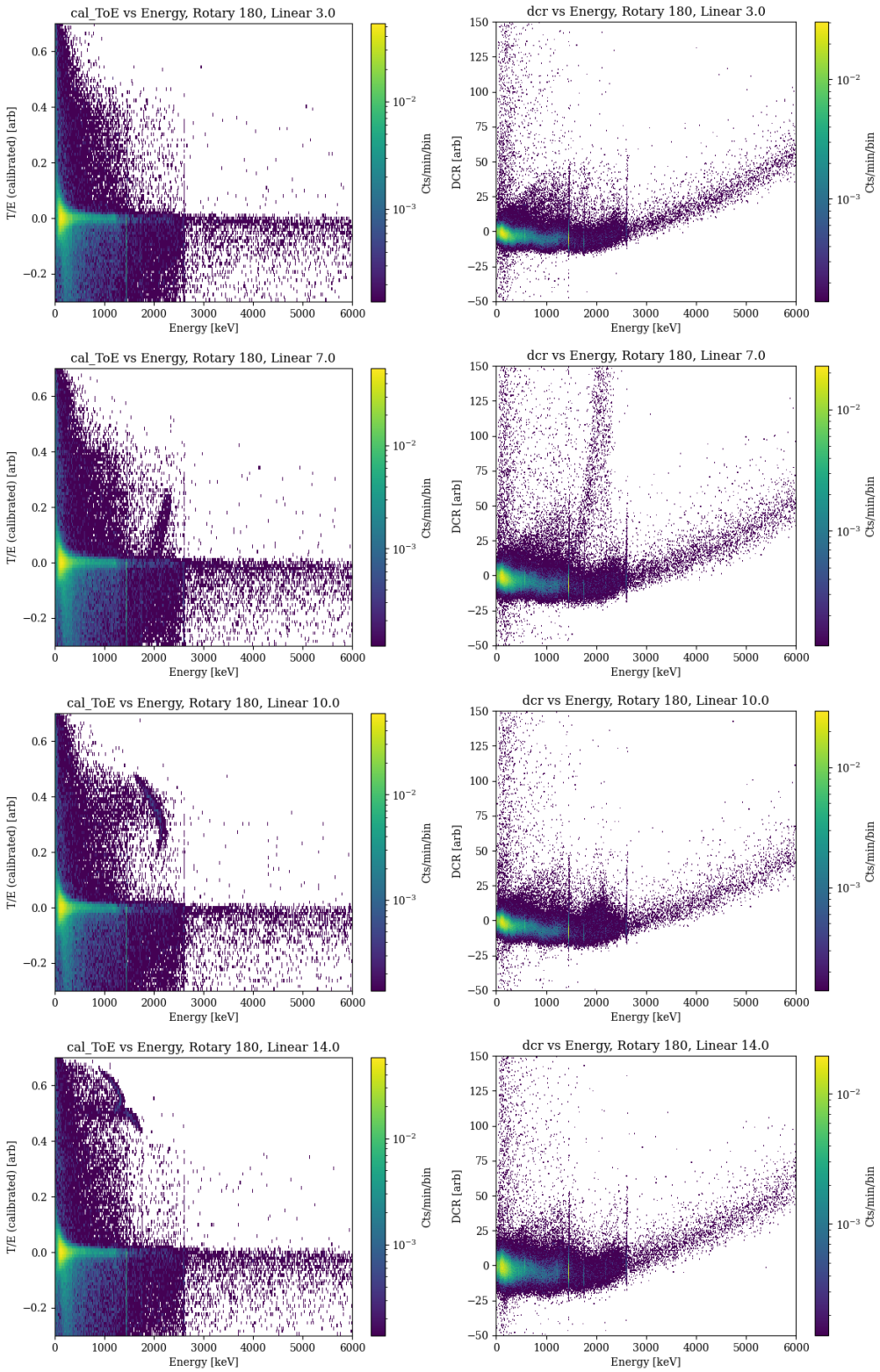

Figure 3.11: T/E *(left)* and DCR *(right)* vs. energy for rotary 180, linear $3, 7, 10, 14$ mm scan positions.

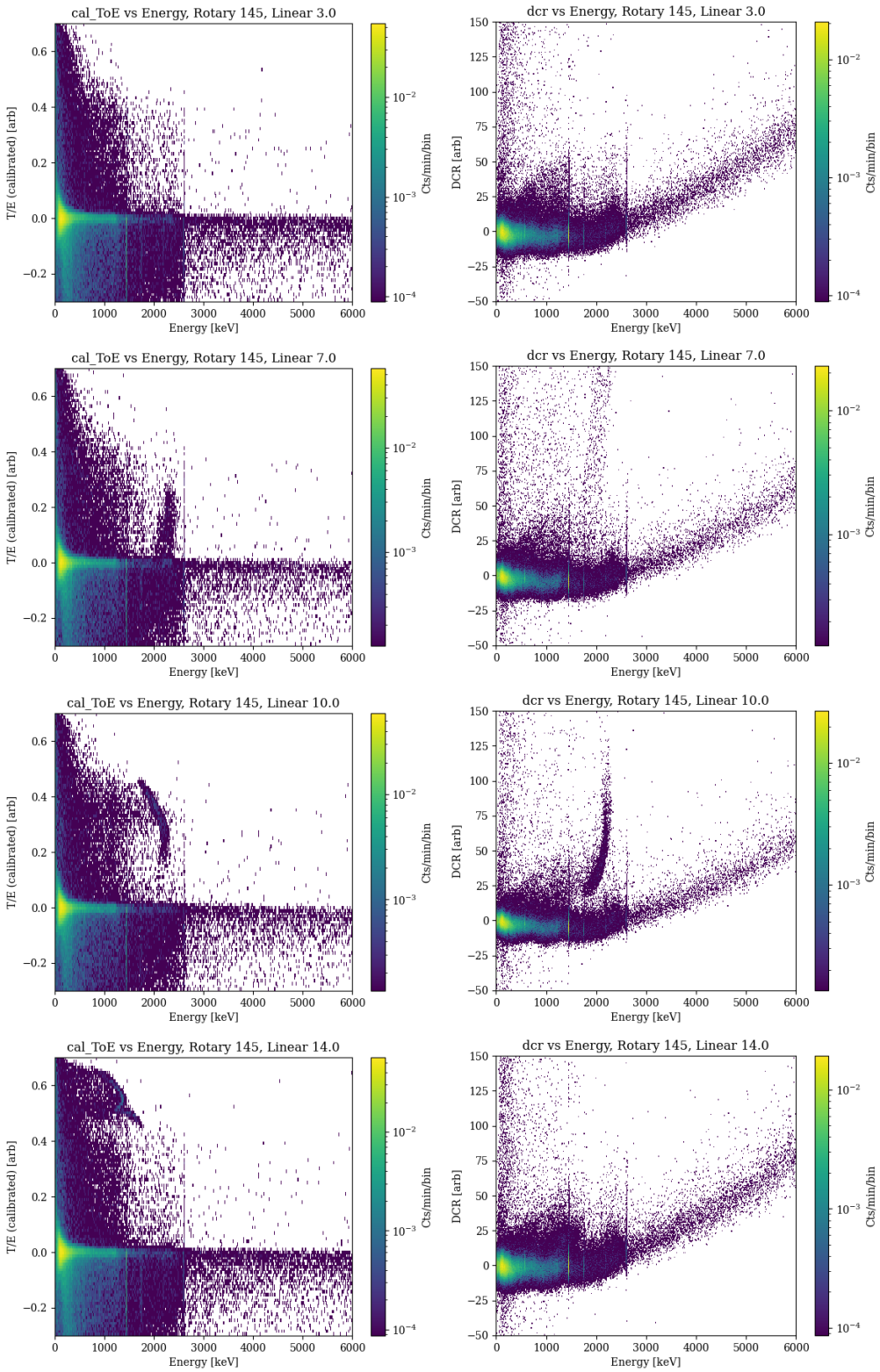

Figure 3.12: T/E *(left)* and DCR *(right)* vs. energy for rotary 145, linear $3, 7, 10, 14$ mm scan positions.

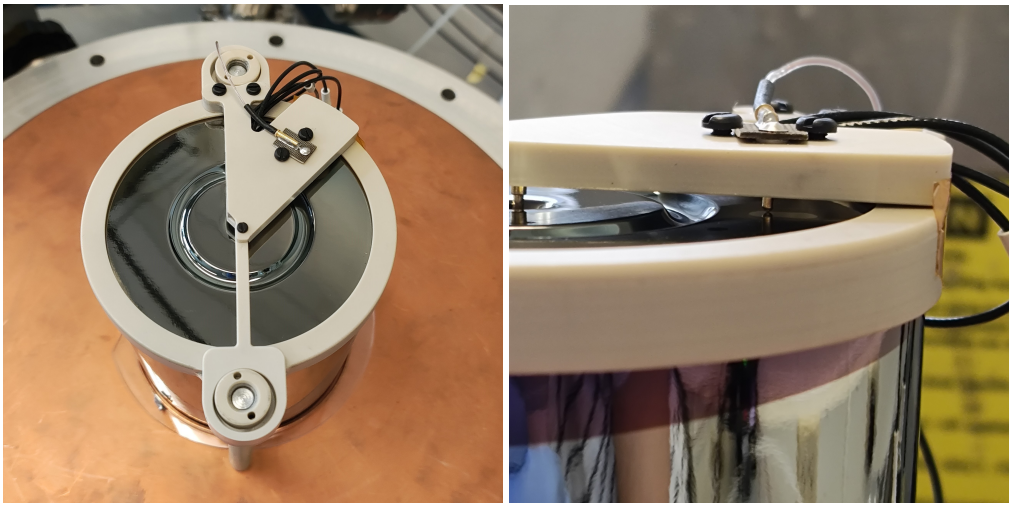

Figure 3.13: Top and side views of the additional PEEK support structures used to make HV contact with the aluminum pad, bypassing the copper HV ring.

factor of 2 higher than the resistance between the front end board and the bonded aluminum pad on the n+ surface (visible in Fig. 3.2. This increased resistance could lead to increased noise in our waveforms.

A new front end holding bridge was created with an additional wing to establish a connection to the aluminum HV pad, shown in Fig. 3.13. A socket for the HV connection is placed on a circuit board, which is fixed with nylon screws to the PEEK wing. A pogo pin is soldered on to the underside of the board to make contact with the aluminum pad.

Data was taken with this HV configuration with a bias voltage of 3400 V. The source was positioned at the rotary 0 position between radii of 0 mm and 14 mm in 2 mm increments. The bias voltage was then increased to 3700 V, and data was retaken at $6, 8, 10,$ and 12 mm. The noise was measured by taking the standard deviation of the first 1000 samples of each waveform. The distribution of this noise is shown in Fig. 3.14 for each dataset as well as for the data analyzed in Section 3.4. The timestamps for each waveform recorded by the digitizer are measured in seconds from the start of each cycle file. To obtain a universal timestamp, the starting time of each cycle is defined to be the timestamp of the last recorded waveform in the previous cycle. Thus, cycle 0 in a dataset will run from time 0 to t_0, and cycle 1 will have times from t_0 to $t_0 + t_1$, and the cycle i will have times from $\sum_{j=0}^{i-1} t_j$ to $\sum_{j=0}^{i} t_j$. This does not account for the fact that there may be minutes to hours of real time between runs. For this study, the noise remains fairly consistent from run to run, so this does not necessarily impact the interpretation of these results. Its relevance will be

discussed more in Section 3.5.2.

The average noise with the copper HV ring was 2.4 keV, with much larger waveform-to-waveform variation, while the average noise with the aluminum pad was 0.9 keV for both bias voltages. There are, however, many systematics that impact noise. For example, the temperature in the aluminum pad data was about 2 K lower than in the full scan, and required less recovery time to the baseline temperature after a source repositioning, as shown in Fig. 3.4. Thus, the exact contribution of this new connection on the average noise cannot necessarily be quantified. However, the consistency between the two runs, especially considering the detector was biased down between the two datasets with the aluminum pad, is promising. The only drawback of this HV connection method is that the additional hardware occludes more of the passivated surface. The rotary 0 and rotary 180 positions, however, should remain unaffected.

3.5.2 Gain Stability

When determining the calibration constants for CAGE data, it became immediately obvious that the gain of our signals was changing significantly between runs. The fact that these jumps in gain were perfectly lined up with changing source positions implied that this was a physical effect due to the movement of the system. This was hypothesized to be due to the shifting of the copper IR shield surrounding the detector impacting the electric fields generated within the detector. A "copper can" was proposed to shield the detector from these effects, acting as a Faraday cage. It cannot be a true Faraday cage, however, because the alpha beam would be unable to penetrate more than $\mathcal{O}(10)$ μm of copper. Instead, a sheet of copper was rolled into a cylinder open at both ends and had tabs welded to the side to secure it to tapped holes drilled into the cold plate. Figure 3.15 shows a top view of the installed detector and copper can inside the cryostat.

This arrangement of the copper can does not allow the top hat to move more than 3 mm without risking a collision. Thus, for this dataset, the source was positioned at $r = 0, 1, 2, 3, 2, 1, 0$ mm. The detector was biased to 3500 V. The gain stability over time is shown in Fig. 3.16, with the time axis determined following the method described in Section 3.5.1. The vertical lines denote where a run ends, meaning the motors were moved at that point. The copper can data, shown in the bottom plot, was taken over a period of 3 days, with an overnight break at 0.4e13 ns and 0.9e13ns.

The center plot shows a closeup of the full scan data, on a timescale similar to what was taken with

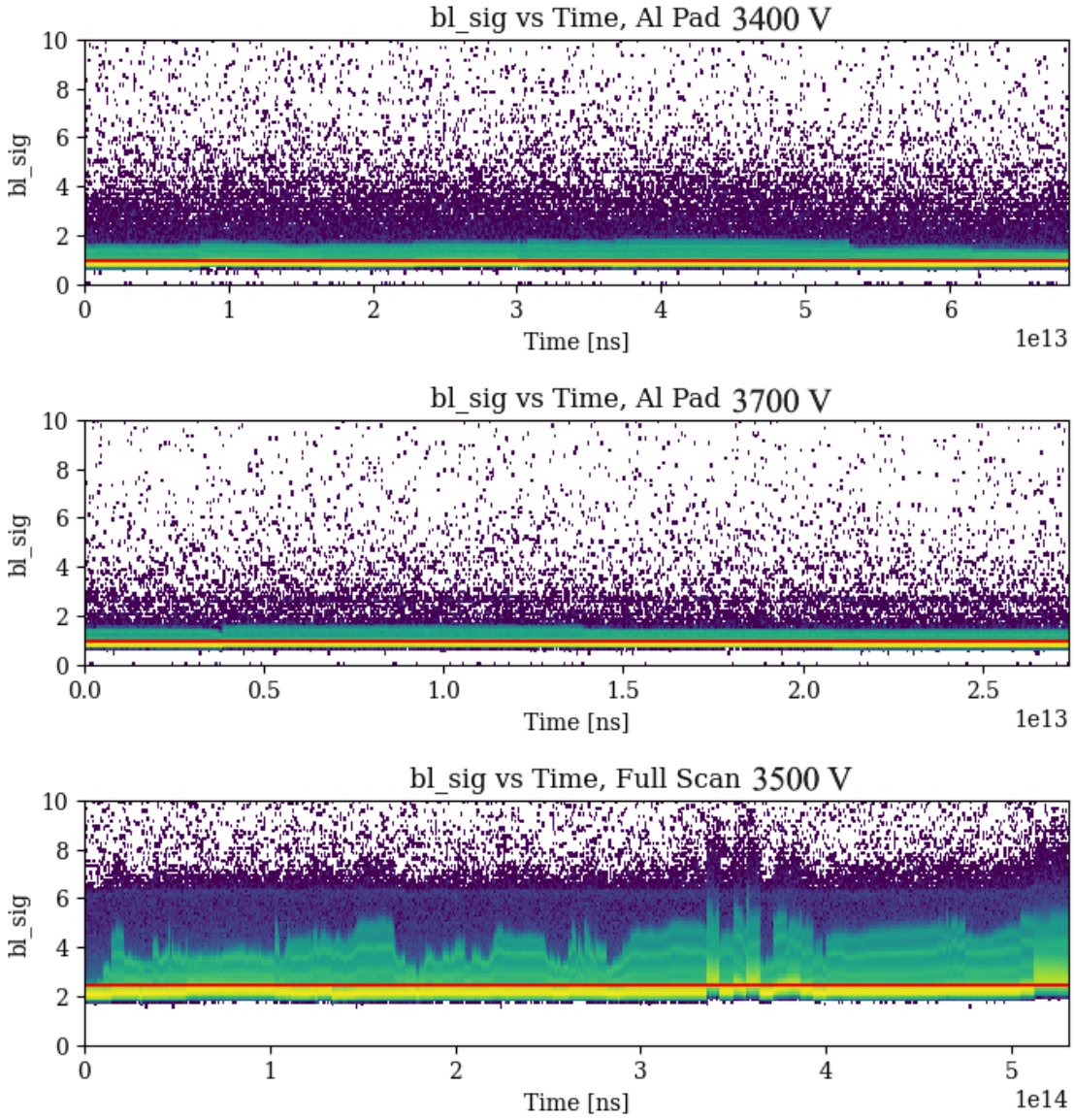

Figure 3.14: 2D histogram of baseline noise over time for data taken with the aluminum pad at 3400 V *(top)* and 3700 V *(middle)* vs. data taken with copper HV ring at 3500 V *(bottom)*. Average values are shown as red horizontal lines.

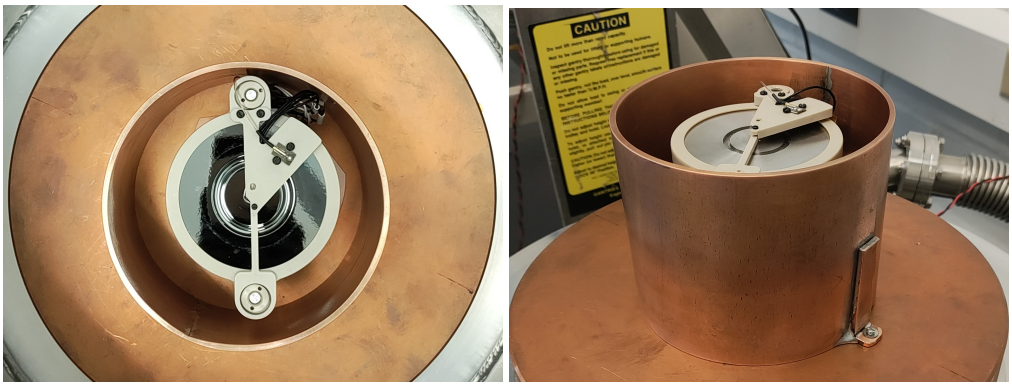

Figure 3.15: Top and side views of the copper can. Tabs screwed into the cold plate ensure good thermal contact.

the copper can. These runs were taken back-to-back, with only a few minutes between to move the source motor, except at the time slightly over 2e13 ns, where a 3 day break in data taking occurred between runs. The radial positions of this data were $r = 14, 12, 10, 9, 8, 7, 6$ mm.

The one large discontinuity remaining in the dataset and the fact that the top hat was moved over a smaller total range of motion leaves us unable to definitively pin the root cause of the gain shifts on changing electric fields. However, the initial comparisons of these runs do imply that the copper can is helping to reduce the size and frequency of these gain shifts. Future work to design a copper can that more closely follows the diameter of the detector and detector holder would restore the top hat's range of motion and is worth pursuing.

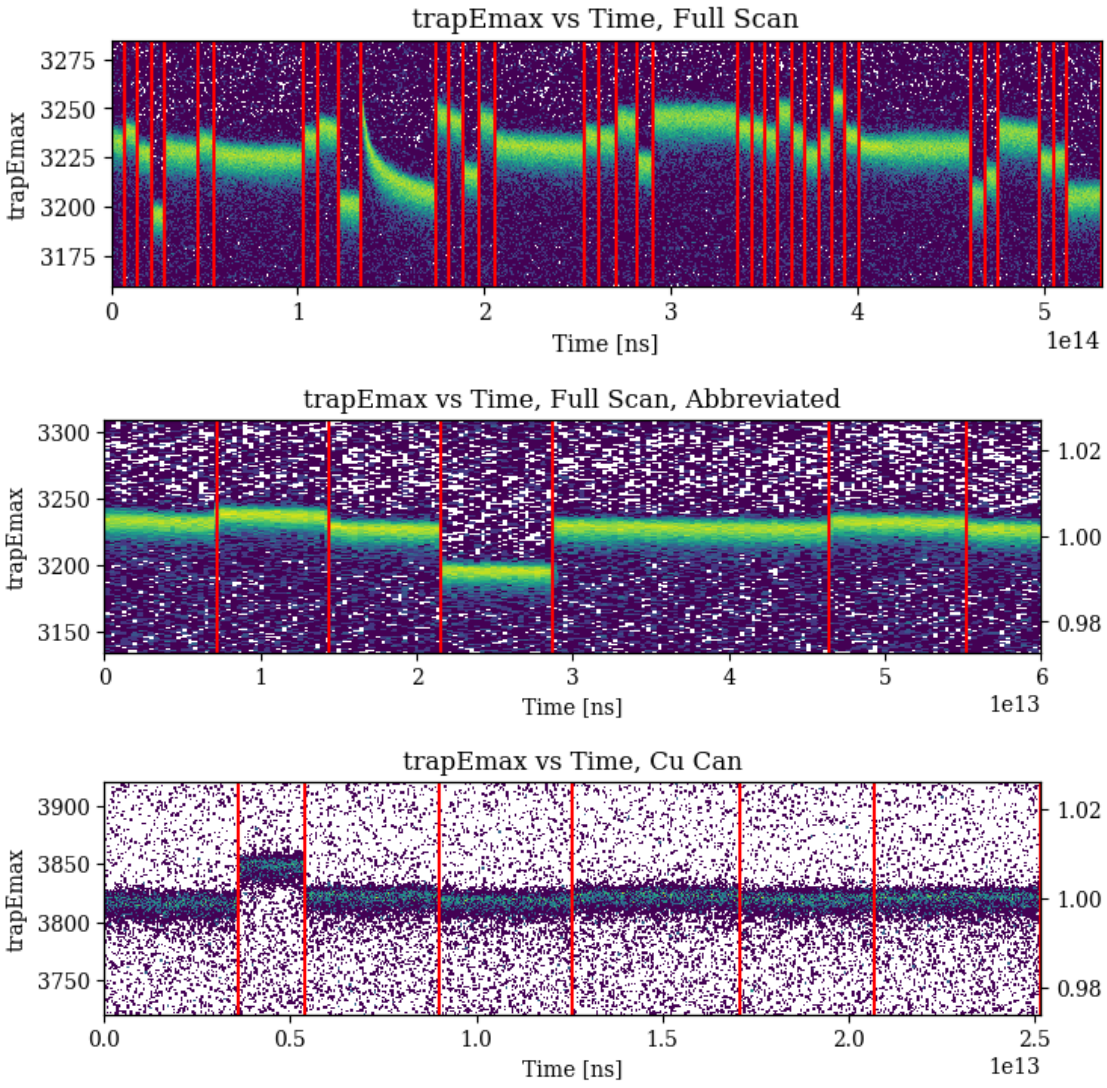

Figure 3.16: Uncalibrated position of the ^{40}K peak over time for the full scan data discussed in Sec. 3.4 (top) and a close up of the full scan data *(middle)* to be more easily compared to data taken with the copper can *(bottom)*. The y-axis labels on the right are normalized by the central value to give percent differences.

Chapter 4

Early Charge Parameter

By identifying alphas using a combination of T/E and DCR, as described in Ch 3, we are able to compare the superpulses of bulk waveforms and the superpulses of alpha waveforms. While the differences in the tail and rising edge are noticeable, the most prominent discrepancy between the two is found in the bottom corner, early in the rising edge, as shown in Fig. 4.1. This is consistent with the pulse shape findings of surface gammas in OPPI, where the time interval between reaching 2% and 20% of the waveform maximum was found to be a good discriminator of 60 keV gamma events from ^{241}Am. This motivated us to create a new PSD parameter that prioritized the early rise of each waveform, which we named early charge (EQ).

4.1 Development and Optimization

We tested multiple calculation methods, including a second derivative, a version of A/E which only viewed the first half of the waveform, and integrals over different intervals. These intervals were between all combinations of `tp_02`, `tp_20`, and `tp_50`, and for fixed intervals of 300 ns to 10 μs before `tp_20`.

First, we identified by eye a few cycles with prominent alpha populations to narrow down the feasible methods. Cycle 4292, taken at a radius of 14mm, has alphas that are well separated in both T/E and DCR, and allows us to verify that they will continue to be visible with our new method. Cycle 4259, taken at a radius of 10mm, has alphas that are not visible in either T/E or DCR and allows us to demonstrate additional discrimination power with our new parameter.

For both of these cycles, we calculated EQ with a variety of methods: integrating the waveform for

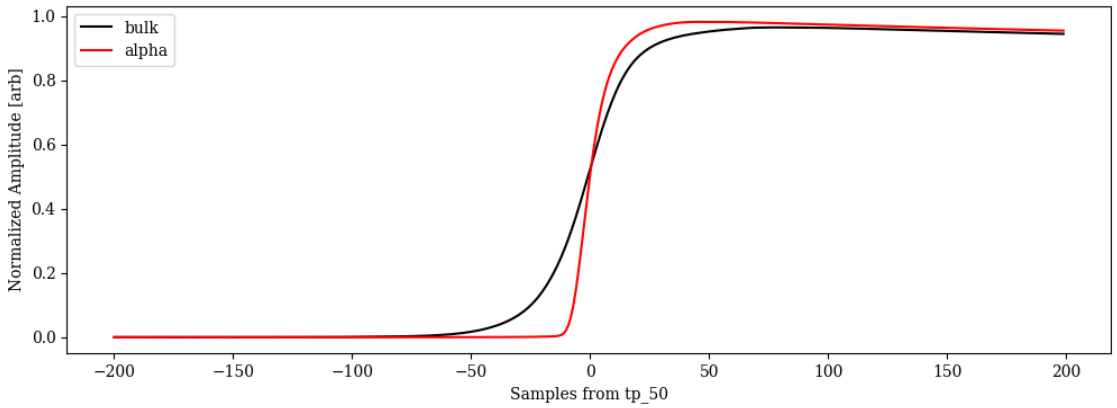

Figure 4.1: Comparison of superpulses for bulk *(black)* events and alpha *(red)* events. Clear differences can be seen in the rising edge. EQ aims to target the differences in the lower corner.

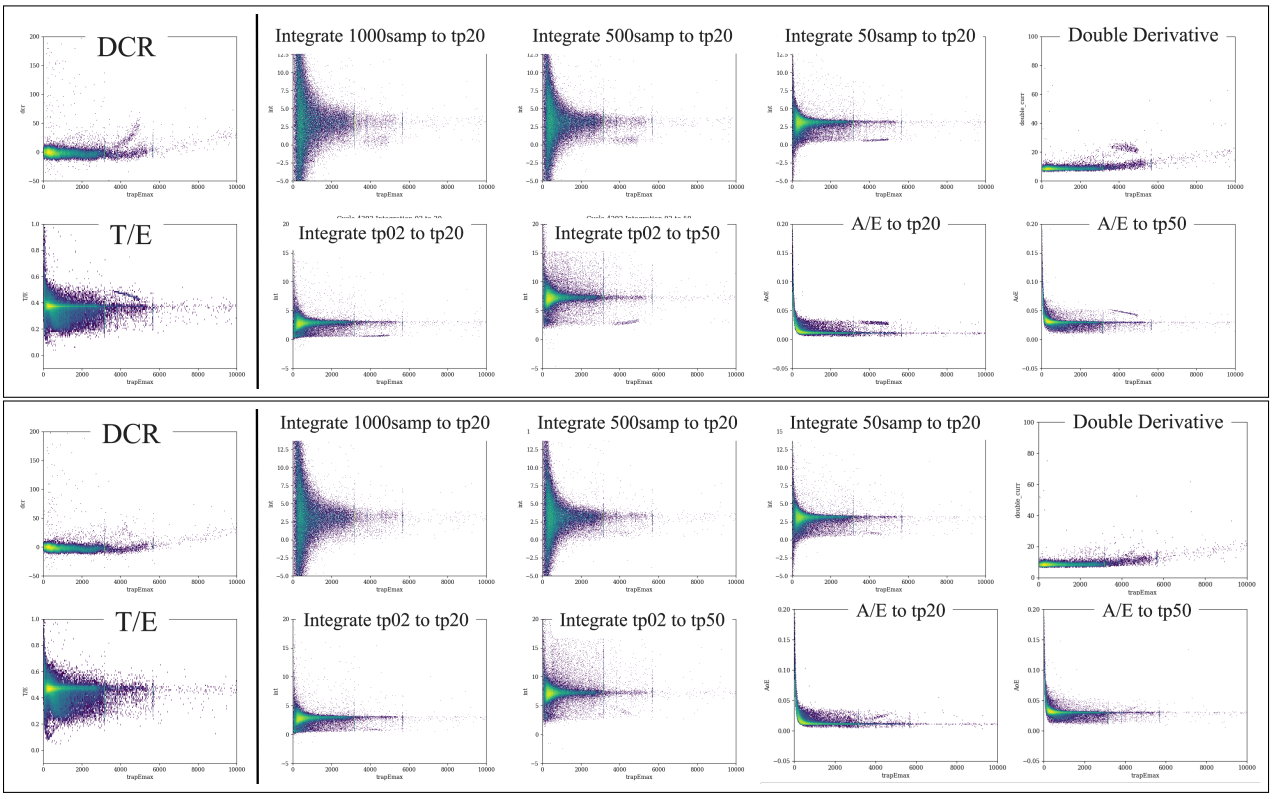

Figure 4.2: The top image is for cycle 4292, which has clearly visible alphas above the bulk distribution. The bottom image is is for cycle 4259, where alphas are not clearly visible in either DCR or T/E. Within each image, to the left of the black line, we show the conventional parameters DCR *(top)* and T/E *(bottom)* vs. uncalibrated energy. To the right of the line, PSD parameter vs. energy for a selection of the PSD parameters investigated as EQ. From left to right, top to bottom, the parameters are integral of 10 μs, 5 μs, and 500 ns before `tp_20`, the maximum of the second derivative, the integral from `tp_02` to `tp_20`, the integral from `tp_02` to `tp_50`, A/E cut off at `tp_20`, and A/E cut off at `tp_50`.

a fixed number of samples before tp_20 or tp_50, integrating the waveforms between tp_02 and tp_20 or tp_50, calculating the second derivate of the waveform, and calculating A/E for a portion of the waveform. The results of these are shown in Fig. 4.2. In cycle 4292, the alphas remained visible in all of the methods shown. In cycle 4259, even though alphas were not visible with the conventional parameters, they become visible in the methods of integrating for a fixed interval before tp_20, between tp_02 and tp_20/ tp_50, and in calculating A/E on a waveform up to tp_20.This narrowed the contenders to the integration methods, and we proceeded to maximize the separation between the alpha and bulk distributions with these methods.

We further narrowed down the methods by finding an optimal fixed time interval to integrate before tp_20. We added an additional cycle, taken at a radius of 16 mm, which had visible alphas in T/E but not DCR and in a lower energy range. For each of these three cycles, we calculated the waveform integral for $300 - 600$ ns, in steps of 50 ns, before tp_20. We then set a cut on each parameter between the bulk distribution and the alphas and performed a Gaussian fit to each population's EQ distribution. A figure of merit (FoM),

$$FOM_{EQ} = \frac{\|\mu_b - \mu_\alpha\|}{\sqrt{\sigma_b^2 + \sigma_\alpha^2}} \tag{4.1}$$

where $\mu_{b/\alpha}, \sigma_{b/\alpha}$ are the fit parameters for the bulk and alpha distributions respectively, is calculated to characterize the separation between the populations. After averaging the FoMs for each cycle, the best integration time was found to be $450 - 550$ ns, so we decided to proceed with a fixed integration time of 500 ns, leaving us with three calculation methods: tp_02 to tp_20, tp_02 to tp_50, and 500 ns ($= 50$ samples) before tp_20.

We then performed each of these calculation methods on a full linear scan. To determine the best method, the T/E and DCR parameters were used to identify a group of bulk events and a group of alpha events in five different scan positions. We then repeated the process of performing a Gaussian fit to the top of each peak and calculating a FoM for each scan position. An example of these fits, for the run at a linear scan position of 10 mm, is shown in Fig. 4.3. The FoM for each method across all linear positions and its average is also shown, with the fixed interval method clearly exhibiting the greatest separation.

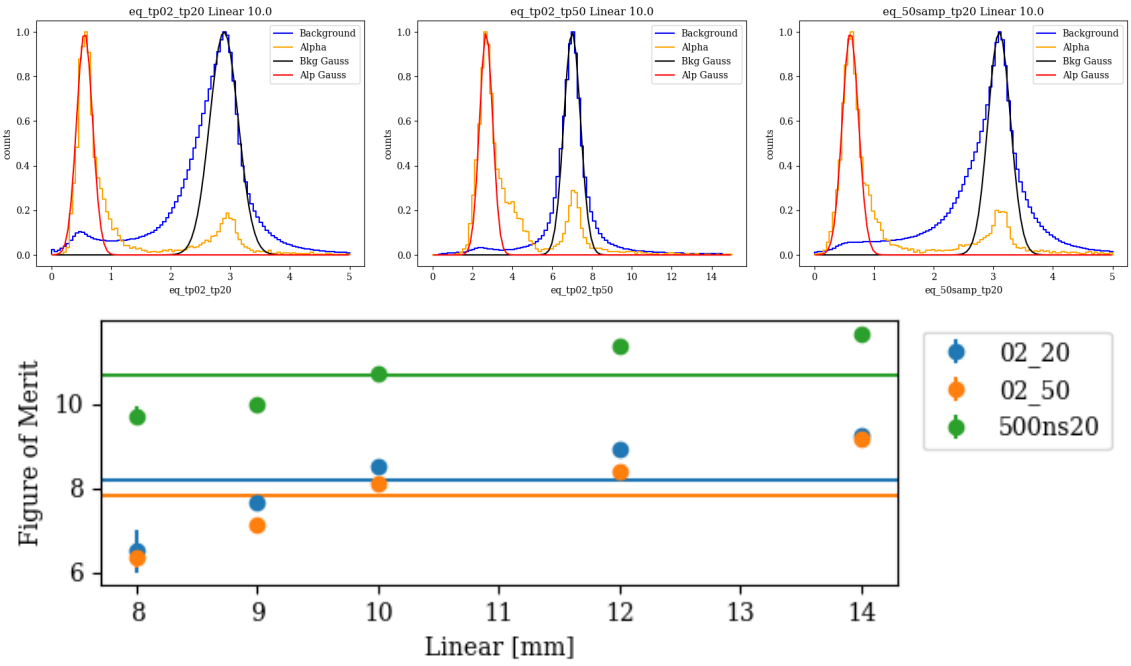

Figure 4.3: *(top)* Normalized background and alpha distributions of each EQ calculation method. The tops of each distribution are fit to a Gaussian and used to calculate a separation figure of merit. The background and alpha distributions are selected with cuts on energy and T/E. The “alpha" population appearing underneath the bulk distribution is believed to be due to less than 100% efficiency in these cuts. *(bottom)* Figure of merit at each linear scan position for each method, with averages shown by horizontal lines.

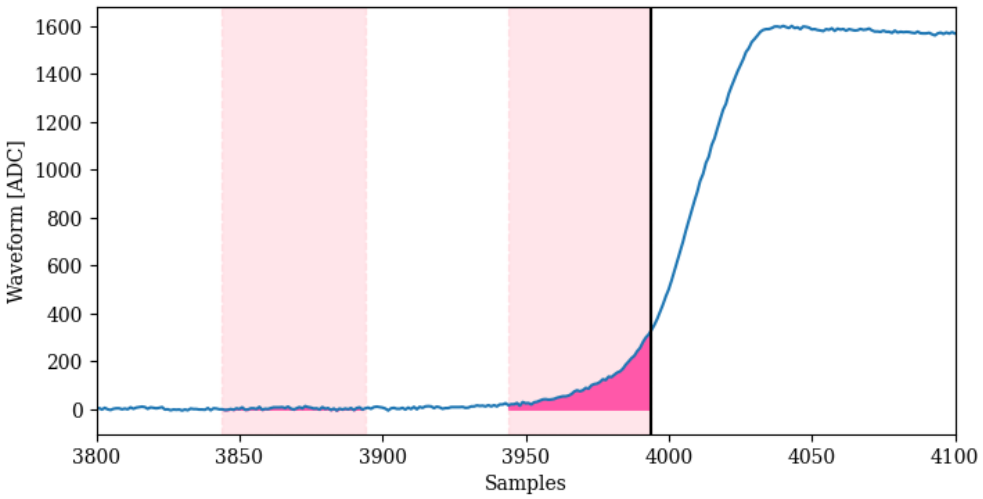

Figure 4.4: Implementation of EQ parameter. Each integration area, shown in pink, is 500 ns long, separated by 500 ns, and the right edge of the later interval lines up with `tp_20`. The integral of the waveform is calculated in each of the pink areas and subtracted from each other to obtain the raw `eq20` value.

4.2 Implementation and Cut Setting

The final implementation of the EQ calculation is the equivalent of a 500 ns integral before `tp_20`, but takes inspiration from LQ and uses a trapezoidal filter to calculate the integral. A rise time and flat time of 500 ns is used, and the value of the trapezoid at `tp_20` is picked off as the raw value of EQ, `eq20`. This allows us to perform the fixed interval integral with an additional baseline subtraction. A visualization of this process is provided in Fig. 4.4.

This value is then normalized by the uncalibrated energy, `trapEmax`, giving us `EQoE`. The distribution of `EQoE` values in background runs is then integrated to produce a discrete CDF. Cuts are placed such that the survival fraction of all background events is 95%, which approximates the point where alpha and background distributions of `EQoE` cross.

4.3 Surface Event Identification Performance

4.3.1 Alpha Events

This cut is applied to both the background and alpha runs, and the alpha rate in the cut events is calculated in the same manner as described in Section 3.4. The difference between the rate of alphas cut by each

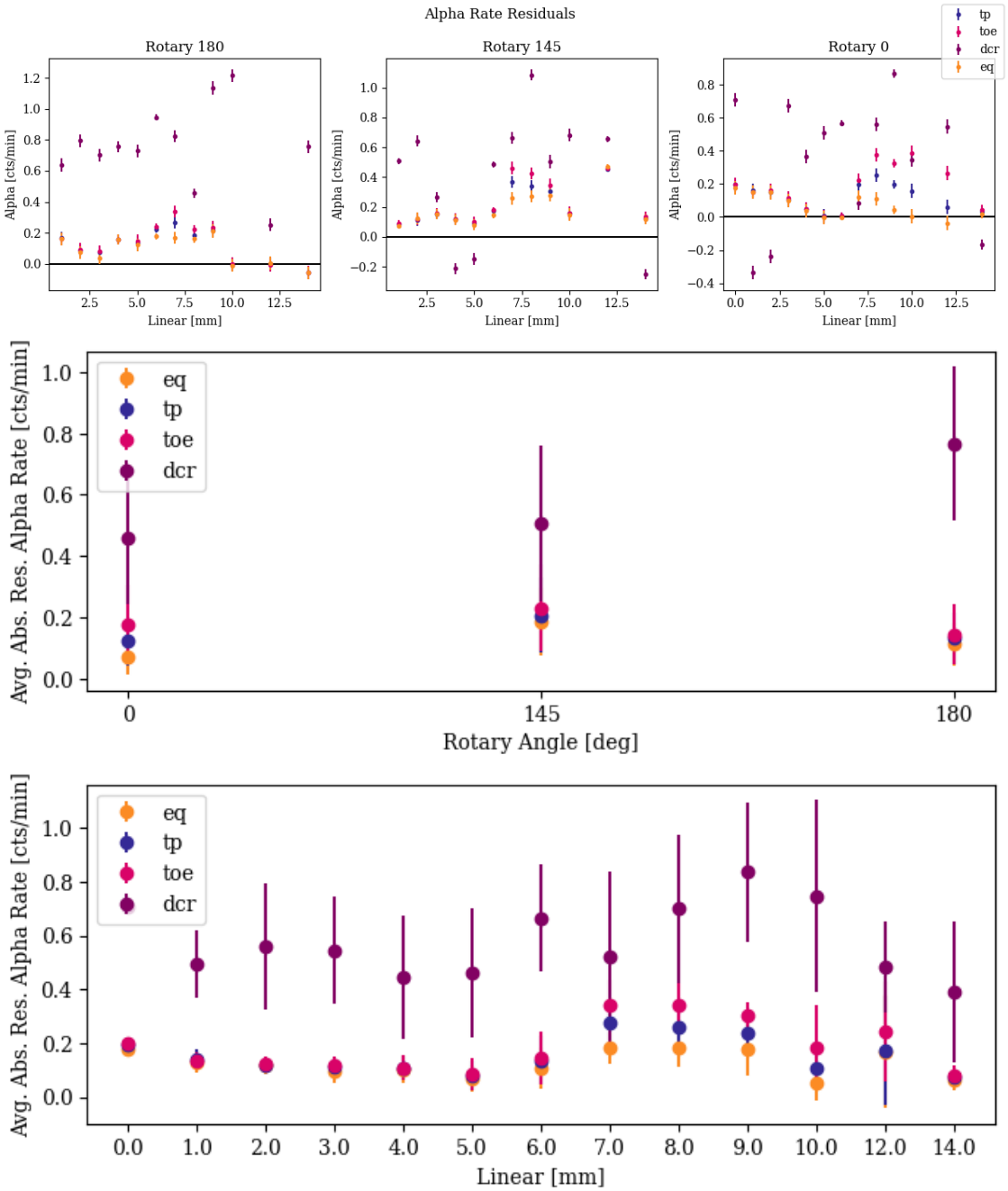

Figure 4.5: Performance of alpha cuts for each of the parameters EQ, T/E, DCR, and `tp_20-tp_02`. The top plot shows the difference between the total alpha rate found in Fig. 3.8 and the alpha rate in the cut events for each parameter. The bottom two plots show the absolute value of that difference, averaged over each rotary or linear position. `EQoE` can be seen to perform the best at each scan position.

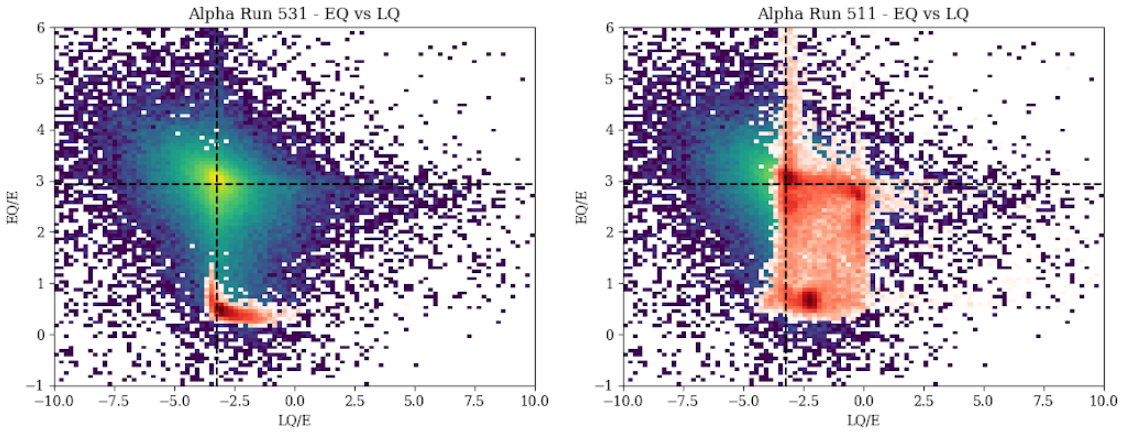

Figure 4.6: Two-dimensional histograms of EQ vs. LQ for two different runs in CAGE. Identical background data is shown in blue-green, while data from events identified as alphas is shown in red. The black dashed vertical line shows the median LQ value in the background data, while the black dashed horizontal line shows the median EQ value in the background data. On the left, the alpha population is shown to be well-separated in EQ, but not in LQ. On the right, a portion of the alpha population is well separated in EQ and a separate portion is well separated in LQ. The separation in EQ appears larger.

parameter at each scan position and the total alpha rate is then calculated and shown as the residual alpha rate for each scan position in Fig. 4.5. A similar procedure is then followed for each of the parameters T/E, DCR, and `tp_20-tp_02`, and the residual alpha rates for each parameter cut is shown in Fig. 4.5, with the average across all linear positions shown by the horizontal lines. The absolute value of this residual, averaged over rotary or linear position, for each parameter is shown in the bottom two plots, and `EQoE` can be seen to outperform the other parameters at all scan positions.

A more qualitative approach was used to compare the performance of EQ against LQ, the surface event cut used in the LEGEND-200 analysis. Two-dimensional histograms of EQ and LQ were made for both background runs and populations identified as alphas through the traditional parameters of T/E and DCR. When applied to data taken in CAGE, two sets of runs emerged. One in which EQ readily identified alphas that LQ missed, and one in which alphas were partially identified by each. In the latter, the alphas identified by EQ appeared to be better separated. Examples of these populations are shown in Fig. 4.6. This serves as motivation that the application of EQ to LEGEND-200 data may be able to cut events in addition to those already cut by the main analysis.

4.3.2 Gamma Events

For the 60 keV gamma events, however, EQoE was less successful at identifying these surface backgrounds. Events with energies 57 keV $< E_{cal} <$ 63 keV were selected. Cuts for each parameter were applied and rates of gamma events were found in the same fashion as the alpha rates, as shown in Fig. 4.7. In this case, tp_20 - tp_02 generally performed the best, except in a handful of scan positions. Looking at the distributions of tp_20 - tp_02 and EQoE for these gamma events, shown in Fig. 4.8, the difference in performance is due to a wider distribution of the EQoE parameter for gamma events, causing some events to fall beyond the cut threshold. This may be, in part, because tp_20 - tp_02 takes discrete values, while EQoE is a continuous distribution. A higher cut threshold for EQoE could be set, at the cost of reducing signal efficiency. A two-dimensional cut on both parameters may also provide better separation between bulk and surface gamma events.

EQoE does have a computational advantage over tp_20 - tp_02, in that it only depends on the determination of one time point. Determining time points, especially ones at low thresholds such as tp_0 and tp_02, is notoriously unstable. This means that EQoE may demonstrate more stable performance, especially in low energy populations.

4.4 Future Work

4.4.1 ^{56}Co

The tradeoff between increased surface event rejection and decreased signal efficiency may be well worth it. Current cuts for EQoE are set to retain a higher percentage of background events than the 90% standard used in LEGEND, and the background events in CAGE are composed of ambient surface radiation, which does not serve as a good proxy for $0\nu\beta\beta$ decay events. A ^{56}Co source would provide multiple double escape peaks at a range of energies, which would provide a high statistics signal-proxy population to more precisely estimate the survival fraction of $0\nu\beta\beta$ decays in these cuts. We produced a 5 μCi ^{56}Co source at CENPA's tandem Van de Graaff accelerator by irradiating an iron foil with a 13 MeV proton beam for this purpose. Future scans using this source could provide better procedures for setting PSD cuts.

This also demonstrates CENPA's ability to produce sources for the LEGEND collaboration as a whole.

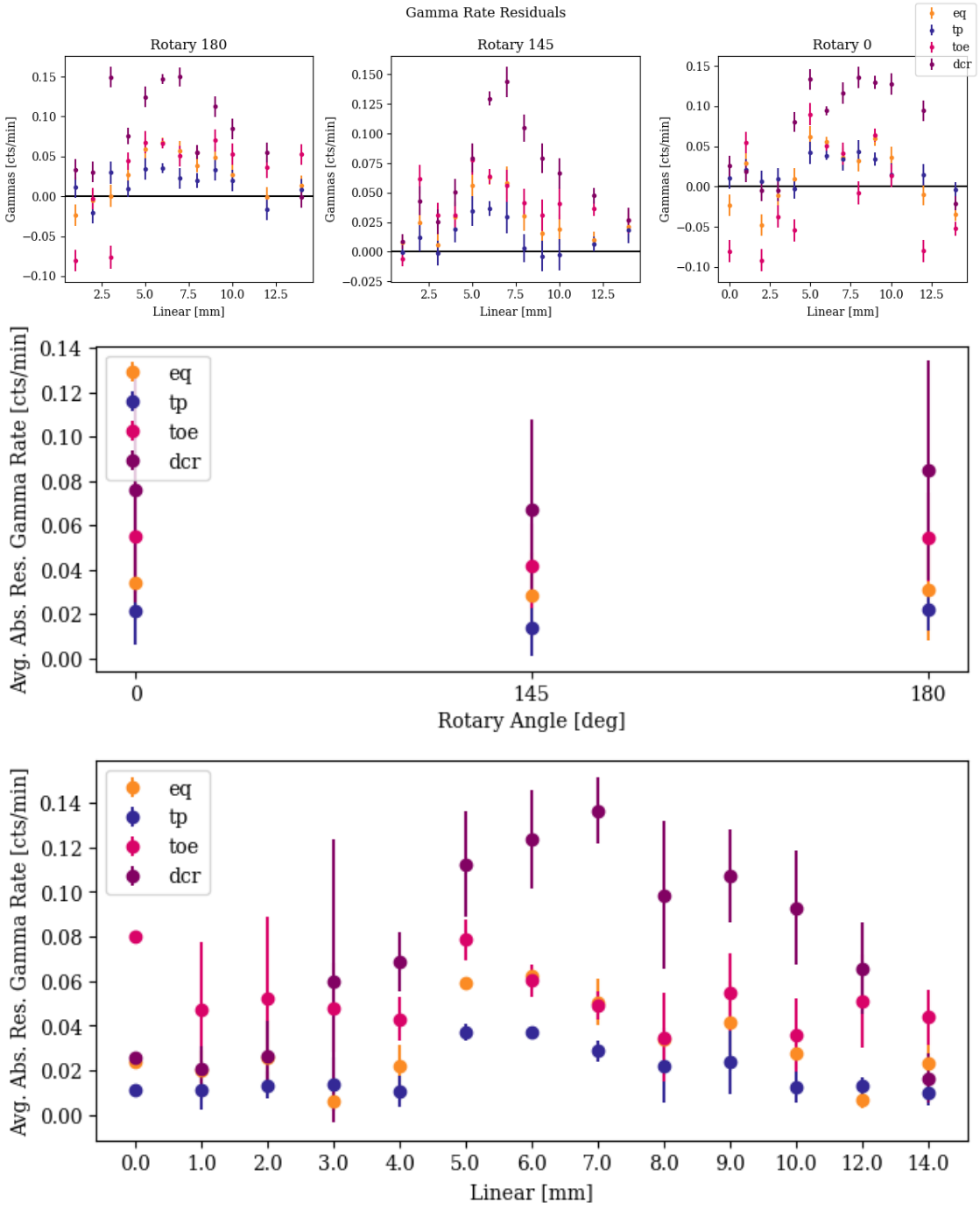

Figure 4.7: Performance of gamma cuts for each of the parameters EQ, T/E, DCR, and `tp_20-tp_02`. The top plot shows the difference between the total alpha rate found in Fig. 3.8 and the alpha rate in the cut events for each parameter. The bottom two plots show the absolute value of that difference, averaged over each rotary or linear position.

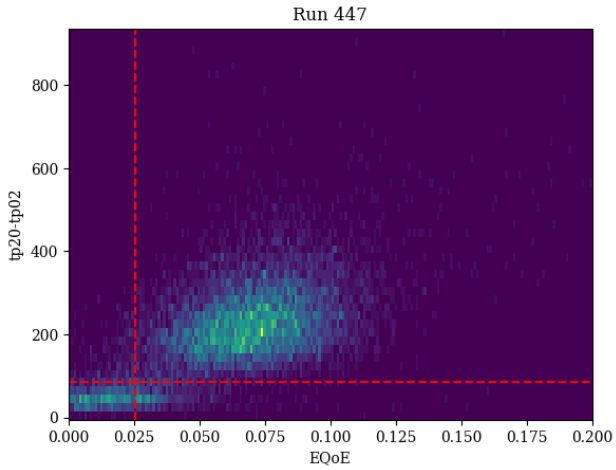

Figure 4.8: `tp_20- tp_02` vs. `EQoE` for events in one CAGE run with energies between 57 keV and 63 keV. The 60 keV gamma events can be seen in the lower left corner. Dashed red lines represent the cut thresholds of each parameter.

^{56}Co has been explored as a calibration source for LEGEND, but raises obstacles with its relatively short 77 day half-life. It cannot be stored for long unless it is produced with very high activity, and a high activity source results in pileup in our detectors. The ability to provide this source on demand would allow for more regular special calibrations to assess the energy dependence of PSD parameters.

4.4.2 Pulse Shape Simulations

In the background distributions of both `EQoE` and `tp_20-tp_02`, a bump can be found on the low side tail. Our current hypothesis for these events is that they come from a volume near the point contact and passivated surface. The events in this bump account for approximately 3% of all events, translating to a region $0.6 - 0.9$ cm deep from the passivated surface and point contact. This hypothesis could be verified through pulse shape simulations.

A simulation suite in Julia, `SolidStateDetectors.jl` [39], provides the ability to customize detector geometry and integrate `Geant4` events to simulate the detector response to a given energy deposition. Accurate pulse shape simulations, however, require accurate understanding of the impurity gradient of the detector. This information was not provided by the manufacturer for the ICPC detector deployed in CAGE. Instead, we follow the procedure outlined in [40] to determine the impurity profile using a measurement of the detector's CV curve.

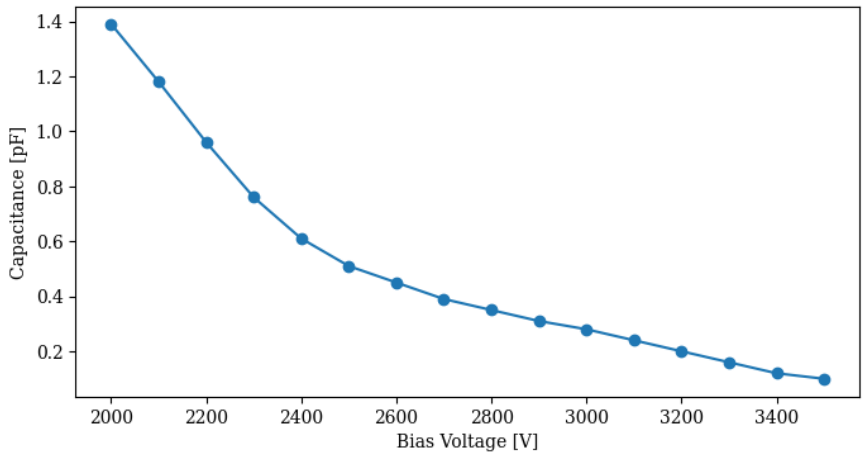

Figure 4.9: Measured CV curve for ICPC

A measurement of the detector's CV curve is made, and a simulated CV curve can be calculated for a given impurity profile. By performing a grid search on the initial impurity and gradient values, the correct impurity profile can then be identified by matching the depletion voltage and slope of the CV curve. OPPI's impurity profile is known, so reproducing its impurity profile will verify the reliability of this method, and these simulations are currently underway. As mentioned in Sec. 3.3.3, measuring the CV curve for CAGE's ICPC detector, shown in Fig. 4.9, suggested that the detector may not be fully depleted, even at 3500 V. When the depletion region stops growing, the capacitance of the detector is expected to stop changing. In this measurement, the CV curve slows but does not stop decreasing, even when reaching a bias voltage that causes an increase in leakage current.

In addition to shining light on the parameter distributions for `EQoE` and `tp_20-tp_02`, further detector simulations may provide answers as to why the T/E behavior is inverted between OPPI and ICPC. Our current hypothesis is that surface charges collecting on the passivated surface can greatly impact pulse shapes. The differing geometry of each detector's passivated surface may influence the charge distributions on its surface.

Chapter 5

EQ in LEGEND-200

EQ showed promise on CAGE data in identifying alphas more reliably than individual conventional parameters. To evaluate its performance in LEGEND-200, we performed a full analysis of the ICPC and PPC detectors included in LEGEND-200's first unblinding dataset.

5.1 Implementation and Calibration

5.1.1 DSP Implementation

The raw `eq20` value is calculated on LEGEND-200 data in the same manner as in CAGE. The 500 ns (corresponding to 31 samples) integral before `tp_20` is calculated with a trapezoidal filter. `EQoE` is then calculated by dividing `eq20` by the uncalibrated `cuspEmax` value.

5.1.2 Calibration Periods

The calibration of EQ is performed on a detector-by-detector basis, with calibration constants determined for each period. The calibration data taken at the beginning of each week-long run is combined over the entire period. This data is then used to determined the calibration constants for physics data taken during that period.

This differs slightly from the calibration scheme used in the LEGEND-200 analysis, where *partitions* are defined for each detector. These partitions evaluate the stability of gain and PSD parameters and may

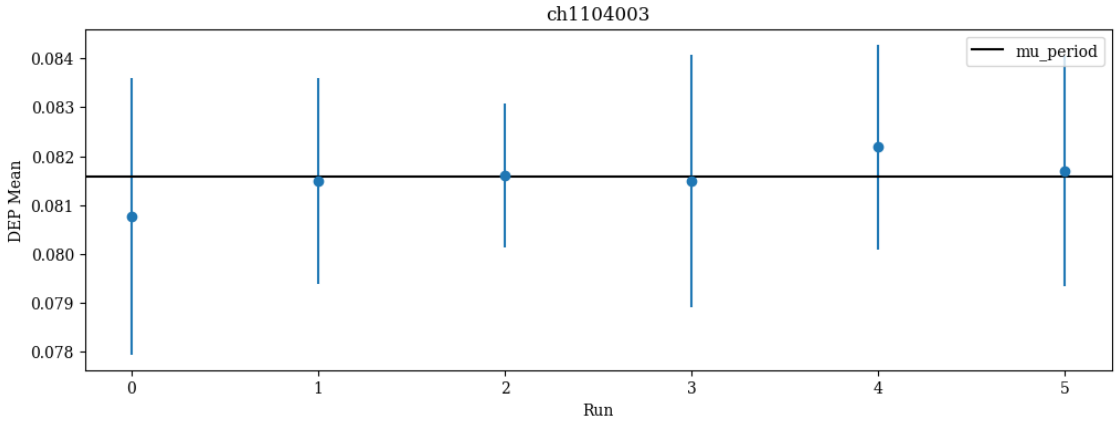

Figure 5.1: Determination of μ_{period} from mean value of DEP `eq20` distribution for one detector in period 6.

combine or split periods. Further studies should be performed to evaluate EQ over the default partitions and determine the optimal periods of stability.

5.1.3 Time Correction

A time correction is made in the style of the LQ calibration [41] by performing a Gaussian fit to the `EQoE` distribution of DEP events for each run in a period to determine the mean value. A calibration constant for the period, μ_{period}, is then calculated as the error weighted average across runs, as shown in Fig. 5.1. The time-corrected parameter EQ_{tcorr} is then calculated as

$$EQ_{tcorr} = \frac{EQoE}{\mu_{period}} \tag{5.1}$$

The distribution for EQ_{tcorr} is thus centered around a value of 1.

5.1.4 Energy Correction

EQ_{tcorr} has an energy-dependent width, shown in Fig. 5.2. The mean also demonstrates slight energy dependence. Both of these are corrected by picking 22 20 keV-wide slices between 100 and 2600 keV, avoiding known gamma lines. A Gaussian fit is performed on the EQ distribution within each energy slice,

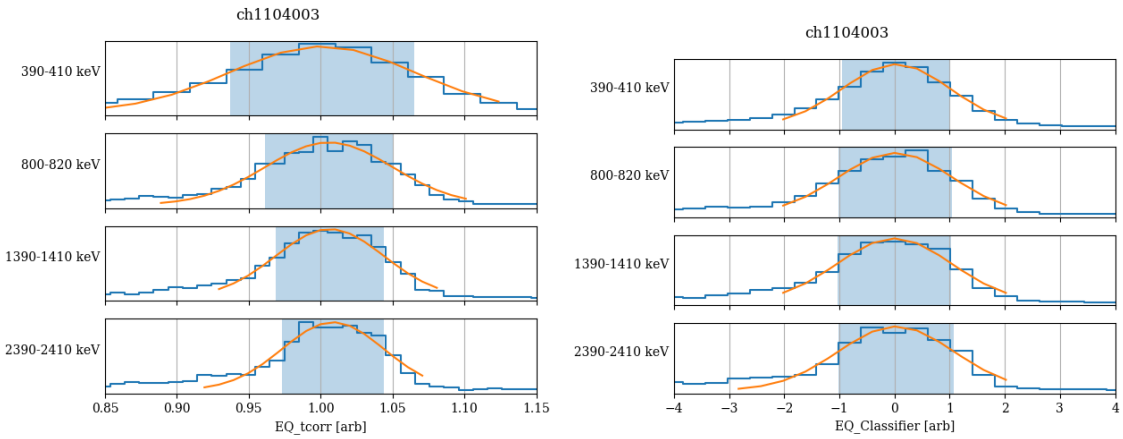

Figure 5.2: EQ before *(left)* and after *(right)* energy correction. The orange curve shows the result of a Gaussian fit, and the shaded blue region represents the $\mu \pm 1\sigma$ region.

and the resultant μ or σ dependence on energy is found by fitting the data to the functions

$$\mu(E) = ae^{-x/b} + c \tag{5.2}$$

$$\sigma(E) = \sqrt{a + \left(\frac{b}{E}\right)^c} \tag{5.3}$$

Then the energy correction is performed by subtracting the $\mu(E)$ dependence and dividing by the $\sigma(E)$ dependence for each event, resulting in a distribution for `EQ_Classifier` centered at 0 with a width of 1.

5.1.5 Setting Cuts

The survival fraction of DEP events is determined for a range of potential `EQ_Classifier` cut values from -20 to 0, evenly spaced by 0.5. The 90% and 95% survival fraction cuts are then determined by linearly interpolating between the tested values, as demonstrated in Fig. 5.3. An event is cut at the x% level if its `EQ_Classifier` value falls below the cut threshold.

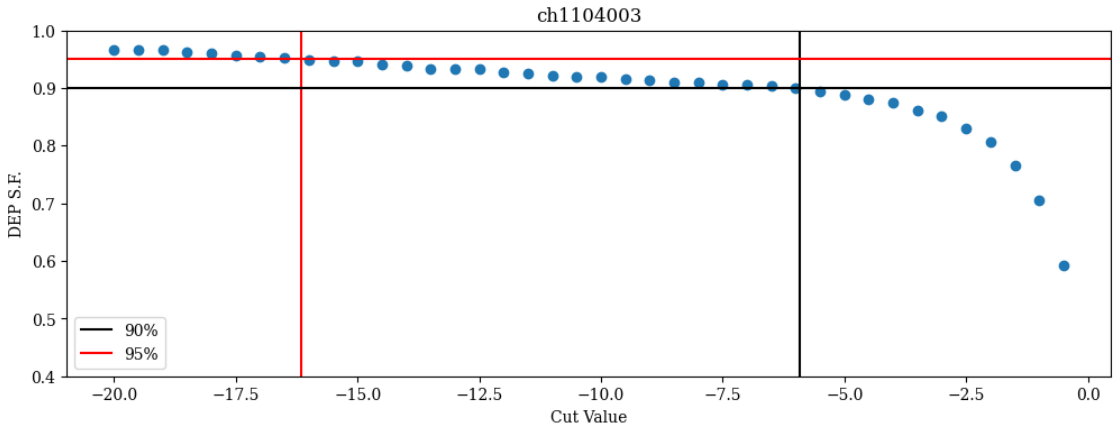

Figure 5.3: DEP survival fraction vs. EQ cut value. 90% and 95% survival fractions cuts are determined by linearly interpolating between values.

5.2 Performance

With a calibrated `EQ_Classifier` parameter and cuts, performance on the initial 61.0 kg yr dataset can be evaluated. EQ has only been applied to ICPC and PPC geometry detectors, totaling 42.3 kg yr, and the analysis in this chapter will be restricted to those channels.

While the cut threshold is determined with respect to the ^{208}Tl DEP survival fraction, we can use the $2\nu\beta\beta$ spectrum as another proxy for $0\nu\beta\beta$-like events. The $2\nu\beta\beta$ spectrum has the advantage of being spread evenly throughout the volume of the detector, unlike the DEP events which are more likely to occur in corners. We define this population as events with energy $1000 - 1300$ keV that pass multiplicity and low A/E cuts. We would like to preserve a high survival fraction of these events.

Another interesting population to examine are alpha events. We define this population as events with energy $3000 - 6000$ keV that pass multiplicity and low A/E cuts. EQ, LQ, and high A/E were all developed to cut surface events, including alphas, so the survival fraction of these events should be close to 0.

The final energy region that we will consider is the analysis window, defined as $1930 - 2190$ keV, with a 50 keV blinded region centered around $Q_{\beta\beta}$ and 10 keV exclusion regions around the known gamma lines of ^{214}Bi and the single escape peak of ^{208}Tl.

To fairly compare the performance of each cut, we must take into account that out of the 43 ICPC and PPC detectors that EQ is applied to, only 18 detectors use LQ and 30 ICPC detectors use high A/E to cut surface events. Survival fractions are calculated relative to these appropriate populations and shown in Table

Cut	$2\nu\beta\beta$	α	Analysis Window
LQ	$2611 \rightarrow 2462$ (94.3%)	$15 \rightarrow 9$ (60.0%)	$7 \rightarrow 0$ (0%)
High A/E	$12732 \rightarrow 12176$ (95.6%)	$167 \rightarrow 0$ (0%)	$18 \rightarrow 4$ (22.2%)
EQ 90	$14046 \rightarrow 12229$ (87.1%)	$168 \rightarrow 0$ (0%)	$24 \rightarrow 5$ (20.8%)
EQ 95	$14046 \rightarrow 12966$ (92.3%)	$168 \rightarrow 0$ (0%)	$24 \rightarrow 6$ (25%)
Current Cuts	$\mathbf{14046 \rightarrow 13590}$ (**96.8%**)	$168 \rightarrow 0$ (0%)	$24 \rightarrow 4$ (16.7%)
LQ + EQ 90	$14046 \rightarrow 12138$ (86.4%)	$168 \rightarrow 0$ (0%)	$\mathbf{24 \rightarrow 3}$ (**12.5%**)
Current Cuts + EQ 90	$14046 \rightarrow 12116$ (86.3%)	$168 \rightarrow 0$ (0%)	$\mathbf{24 \rightarrow 3}$ (**12.5%**)
Current Cuts + EQ 95	$14046 \rightarrow 12809$ (91.2%)	$168 \rightarrow 0$ (0%)	$24 \rightarrow 4$ (16.7%)

Table 5.1: Number (percentage) of events in each region that survive each cut combination. The LQ cut is only applied to PPC detectors while the high A/E cut is only applied to ICPC detectors, resulting in different total populations for each cut. The bolded values in each column show the cuts with the best performance in each population.

5.1 in the format "Total Population $\rightarrow$ Surviving Population (Survival Percentage)."

In particular, the usage of EQ 90 in place of high A/E cuts one additional event in the analysis window. The details of this event are shown in Fig. 5.4. The fast early rise is clearly visible in the waveform even though its A/E value does not reflect this. A surface event would need a value of A/E > 3 to be cut, while this event actually has a negative value of A/E. This additional cut event, however, comes at a cost of over 10% decrease in the $2\nu\beta\beta$ survival fraction. A higher survival fraction of DEP events compared to $2\nu\beta\beta$ decay events is consistent with the theory, discussed in Sec. 4.4.2, that the low EQ bump seen in CAGE corresponds to a volumetric population close to the passivated surface. This is further corroborated when the $2\nu\beta\beta$ events are broken down by detector type. PPC detectors, with their large passivated surfaces, have a lower survival fraction of $1090/1314 = 0.830$ compared to the ICPC survival fraction of $11139/12732 = 0.875$.

The EQ parameter was developed to cut surface events based on their distinctive rising edge. This essentially led to the development of a volumetric cut of events that originate near the passivated surface and p+ contact, where the weighting potential changes rapidly. The cut threshold for this parameter is tunable and can be set to cut additional background in LEGEND-200, at the cost of significant signal efficiency. The fact that the other events remaining in the analysis window are not cut by the EQ parameter also teaches us that they are most likely not surface events and that other techniques need to be used to identify and remove those backgrounds.

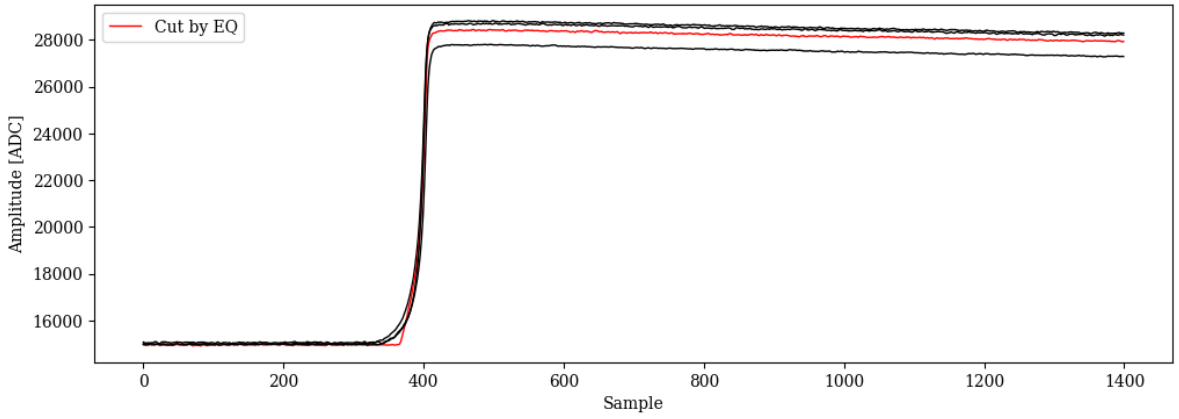

Timestamp	Detector	Energy [keV]	LQ	A/E	EQ	EQ 90% Cut	EQ 95% Cut
12-18-2023 01:58	V07647A	1953.14	-1.42	-0.46	-8.02	-4.74	-13.95

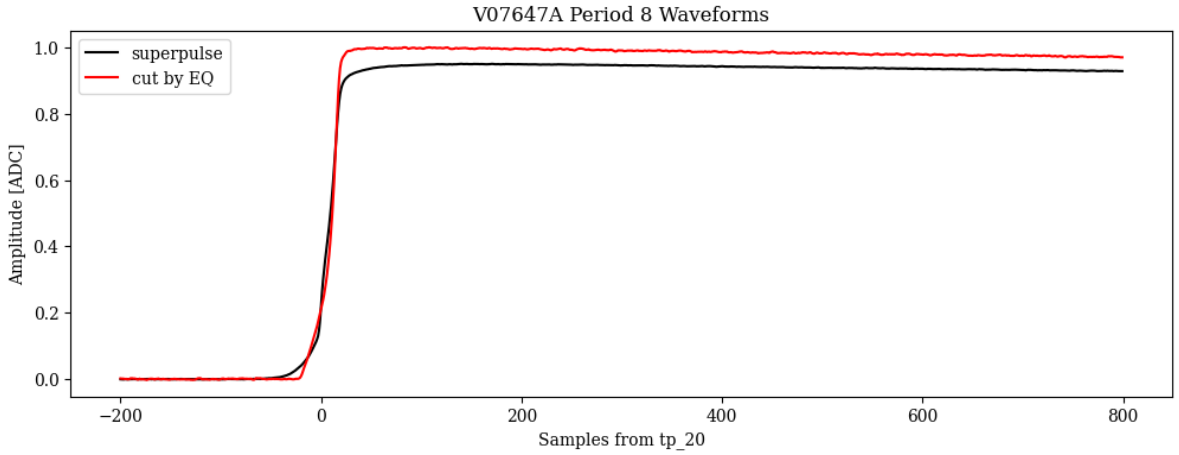

Figure 5.4: *(top)* Waveforms for events that survive LQ and A/E cuts. The additional event cut by EQ is plotted in red. *(middle)* Energy and PSD values for the event cut by EQ. *(bottom)* Cut event waveform compared to superpulse of waveforms in its period, aligned at `tp_20`.

Chapter 6

Conclusion

6.1 The CAGE Scanner

In this work, we document the use of the CAGE scanner to characterize high purity germanium detectors used in the search for $0\nu\beta\beta$ decay with LEGEND. Improvements to the alignment of CAGE, hardware modifications to accommodate larger, more modern detector geometries, and exploratory improvements to noise and stability performance were made. We undertook dedicated scans to study the behavior of surface events, including alphas and low energy gammas, and showed that detector response to these events differs between ICPC and PPC geometries in conventional pulse shape discrimination parameters used to reject surface backgrounds.

Further scans could be performed with the CAGE test stand, in particular, scans of the passivated ditch on ICPC's surface to compare behavior of radiation entering the ditch to radiation entering other points on the passivated surface. CAGE's unique source alignment system also allows us to perform incidence angle scans of the passivated surface, analyzing the relation between PSD performance and penetration depth of alphas.

6.2 Early Charge

Alpha scans performed with the CAGE scanner led to the development of a new pulse shape discrimination parameter, Early Charge (EQ), a measure of the risetime of the first 20% of the waveform signal. EQ

demonstrates more stable performance and higher rates of alpha identification regardless of detector position than conventional PSD parameters used in recent $0\nu\beta\beta$ decay searches in ^{76}Ge.

Its promising performance on CAGE alpha scan data prompted the investigation of EQ's performance on LEGEND-200 data. Application of an EQ cut set at a 90% survival fraction for DEP events to ICPC and PPC detectors resulted in the rejection of one additional event in the analysis window, at the cost of a 10% drop in the survival fraction in the $2\nu\beta\beta$ decay spectrum.

6.3 Future Directions

More investigations should be performed to quantify the efficiency of the EQ cut and trade-offs between increased surface event rejection with any loss in exposure. New calibration techniques that can evaluate survival fractions on spatially homogeneous populations would also benefit the EQ analysis. The production of ^{56}Co sources and its use as a calibration source in both LEGEND-200 and CAGE would allow studies of efficiency as a function of energy.

Pulse shape simulation studies would also shine light on the nature of events cut by EQ and impacts of detector geometry on cut performance. These simulations could be compared to CAGE ICPC scans shown in this work, as well as retroactively applied to PPC geometry scans. Comparisons can also be made to LEGEND-200 data, which includes BEGe detectors as well, which share similar passivated surface geometries to ICPC detectors, but have smaller volumes. These simulations will be made possible by determination of the ICPC impurity gradient, which first requires closer examination of the depletion behavior of the detector and may suffer from degeneracies in the CV curve generated by a given impurity gradient. Other work in germanium has shown a large influence of surface charge on detector behavior, and further development of `SolidStateDetectors.jl` to include surface charge modelling would also allow more detailed simulations of germanium detectors.

These studies of low EQ events aim to improve our understanding of detector performance and increase our confidence that backgrounds are being adequately rejected in the search for $0\nu\beta\beta$ decay.

Bibliography

[1] Yanagida T. Fukugita, M. *Physics of Neutrinos and Applications to Astrophysics*. Springer-Verlag Berlin Heidelberg New York, 2003.

[2] F. Reines and C. Cowan. The Reines-Cowan experiments: Detecting the Poltergeist. *Los Alamos Sci.*, 25:4–27, 1997.

[3] H. A. Bethe and R. F. Bacher. Nuclear physics a. stationary states of nuclei. *Rev. Mod. Phys.*, 8: 82–229, Apr 1936. doi: 10.1103/RevModPhys.8.82. URL https://link.aps.org/doi/10.1103/RevModPhys.8.82.

[4] C. S. Wu, E. Ambler, R. W. Hayward, D. D. Hoppes, and R. P. Hudson. Experimental test of parity conservation in beta decay. *Phys. Rev.*, 105:1413–1415, Feb 1957. doi: 10.1103/PhysRev.105.1413. URL https://link.aps.org/doi/10.1103/PhysRev.105.1413.

[5] S. Navas et al. Review of particle physics. *Phys. Rev. D*, 110(3):030001, 2024. doi: 10.1103/PhysRevD.110.030001.

[6] Raymond Davis. A review of the homestake solar neutrino experiment. *Progress in Particle and Nuclear Physics*, 32:13–32, 1994. ISSN 0146-6410. doi: https://doi.org/10.1016/0146-6410(94)90004-3. URL https://www.sciencedirect.com/science/article/pii/0146641094900043.

[7] T. J. Haines, R. M. Bionta, G. Blewitt, C. B. Bratton, D. Casper, R. Claus, B. G. Cortez, S. Errede, G. W. Foster, W. Gajewski, K. S. Ganezer, M. Goldhaber, T. W. Jones, D. Kielczewska, W. R. Kropp, J. G. Learned, E. Lehmann, J. M. LoSecco, J. Matthews, H. S. Park, L. R. Price, F. Reines, J. Schultz,

S. Seidel, E. Shumard, D. Sinclair, H. W. Sobel, J. L. Stone, L. Sulak, R. Svoboda, J. C. van der Velde, and C. Wuest. Calculation of atmospheric neutrino-induced backgrounds in a nucleon-decay search. *Phys. Rev. Lett.*, 57:1986–1989, Oct 1986. doi: 10.1103/PhysRevLett.57.1986. URL https://link.aps.org/doi/10.1103/PhysRevLett.57.1986.

[8] Masayuki Nakahata, Katsushi Arisaka, Takaaki Kajita, Masatoshi Koshiba, Yuichi Oyama, Atsuto Suzuki, Masato Takita, Yoji Totsuka, Tadashi Kifune, Teruhiro Suda, Nobuaki Sato, Kasuke Takahashi, and Kazumasa Miyano. Atmospheric neutrino background and pion nuclear effect for kamioka nucleon decay experiment. *Journal of the Physical Society of Japan*, 55(11):3786–3805, 1986. doi: 10.1143/JPSJ.55.3786. URL https://doi.org/10.1143/JPSJ.55.3786.

[9] Y. Fukuda et al. Evidence for oscillation of atmospheric neutrinos. *Phys. Rev. Lett.*, 81:1562–1567, 1998. doi: 10.1103/PhysRevLett.81.1562.

[10] Alan W. P. Poon et al. Neutrino observations from the Sudbury Neutrino Observatory. *AIP Conf. Proc.*, 610(1):218–230, 2002. doi: 10.1063/1.1469931.

[11] T. Araki, K. Eguchi, S. Enomoto, K. Furuno, K. Ichimura, H. Ikeda, K. Inoue, K. Ishihara, T. Iwamoto, T. Kawashima, Y. Kishimoto, M. Koga, Y. Koseki, T. Maeda, T. Mitsui, M. Motoki, K. Nakajima, H. Ogawa, K. Owada, J.-S. Ricol, I. Shimizu, J. Shirai, F. Suekane, A. Suzuki, K. Tada, O. Tajima, K. Tamae, Y. Tsuda, H. Watanabe, J. Busenitz, T. Classen, Z. Djurcic, G. Keefer, K. McKinny, D.-M. Mei, A. Piepke, E. Yakushev, B. E. Berger, Y. D. Chan, M. P. Decowski, D. A. Dwyer, S. J. Freedman, Y. Fu, B. K. Fujikawa, J. Goldman, F. Gray, K. M. Heeger, K. T. Lesko, K.-B. Luk, H. Murayama, A. W. P. Poon, H. M. Steiner, L. A. Winslow, G. A. Horton-Smith, C. Mauger, R. D. McKeown, P. Vogel, C. E. Lane, T. Miletic, P. W. Gorham, G. Guillian, J. G. Learned, J. Maricic, S. Matsuno, S. Pakvasa, S. Dazeley, S. Hatakeyama, A. Rojas, R. Svoboda, B. D. Dieterle, J. Detwiler, G. Gratta, K. Ishii, N. Tolich, Y. Uchida, M. Batygov, W. Bugg, Y. Efremenko, Y. Kamyshkov, A. Kozlov, Y. Nakamura, C. R. Gould, H. J. Karwowski, D. M. Markoff, J. A. Messimore, K. Nakamura, R. M. Rohm, W. Tornow, R. Wendell, A. R. Young, M.-J. Chen, Y.-F. Wang, and F. Piquemal. Measurement of neutrino oscillation with kamland: Evidence of spectral

distortion. *Phys. Rev. Lett.*, 94:081801, Mar 2005. doi: 10.1103/PhysRevLett.94.081801. URL https://link.aps.org/doi/10.1103/PhysRevLett.94.081801.

[12] X. Qian and P. Vogel. Neutrino mass hierarchy. *Progress in Particle and Nuclear Physics*, 83:1–30, jul 2015. doi: 10.1016/j.ppnp.2015.05.002. URL https://doi.org/10.1016%2Fj.ppnp.2015.05.002.

[13] The DUNE collaboration. Dune phase ii: scientific opportunities, detector concepts, technological solutions. *Journal of Instrumentation*, 19(12):P12005, dec 2024. doi: 10.1088/1748-0221/19/12/P12005. URL https://doi.org/10.1088/1748-0221/19/12/P12005.

[14] Hyper-Kamiokande Proto-Collaboration. Hyper-kamiokande design report, 2018. URL https://arxiv.org/abs/1805.04163.

[15] The JUNO Collaboration. Potential to identify neutrino mass ordering with reactor antineutrinos at juno*. *Chinese Physics C*, 49(3):033104, mar 2025. doi: 10.1088/1674-1137/ad7f3e. URL https://doi.org/10.1088/1674-1137/ad7f3e.

[16] Ettore Majorana and Luciano Maiani. *A symmetric theory of electrons and positrons*, pages 201–233. Springer Berlin Heidelberg, Berlin, Heidelberg, 2006. ISBN 978-3-540-48095-2. doi: 10.1007/978-3-540-48095-2_10. URL https://doi.org/10.1007/978-3-540-48095-2_10.

[17] KATRIN Collaboration. Direct neutrino-mass measurement based on 259 days of katrin data. *Science*, 388(6743):180–185, 2025. doi: 10.1126/science.adq9592. URL https://www.science.org/doi/abs/10.1126/science.adq9592.

[18] M. Fukugita and T. Yanagida. Barygenesis without grand unification. *Physics Letters B*, 174(1):45–47, 1986. ISSN 0370-2693. doi: https://doi.org/10.1016/0370-2693(86)91126-3. URL https://www.sciencedirect.com/science/article/pii/0370269386911263.

[19] M. Drewes, Y. Georis, C. Hagedorn, and J. Klarić. Low-scale leptogenesis with flavour and CP symmetries. *Journal of High Energy Physics*, 2022(12), dec 2022. doi: 10.1007/jhep12(2022)044. URL https://doi.org/10.1007%2Fjhep12%282022%29044.

[20] Neil D. Barrie, Chengcheng Han, and Hitoshi Murayama. Affleck-dine leptogenesis from higgs inflation. *Phys. Rev. Lett.*, 128:141801, Apr 2022. doi: 10.1103/PhysRevLett.128.141801. URL https://link.aps.org/doi/10.1103/PhysRevLett.128.141801.

[21] Matteo Agostini, Giovanni Benato, Jason A. Detwiler, Javier Menéndez, and Francesco Vissani. Toward the discovery of matter creation with neutrinoless $0\nu\beta\beta$ decay. *Reviews of Modern Physics*, 95(2), may 2023. doi: 10.1103/revmodphys.95.025002. URL https://doi.org/10.1103%2Frevmodphys.95.025002.

[22] G. Putnam. Neutrino mass models. URL https://homes.psd.uchicago.edu/~sethi/Teaching/P445-S2019/Gray%20Putnam%20QFT3%20Report.pdf.

[23] Frank T. Avignone, Steven R. Elliott, and Jonathan Engel. Double beta decay, majorana neutrinos, and neutrino mass. *Reviews of Modern Physics*, 80(2):481–516, apr 2008. doi: 10.1103/revmodphys.80.481. URL https://doi.org/10.1103%2Frevmodphys.80.481.

[24] I. J. Arnquist, F. T. Avignone, A. S. Barabash, C. J. Barton, P. J. Barton, K. H. Bhimani, E. Blalock, B. Bos, M. Busch, M. Buuck, T. S. Caldwell, Y-D. Chan, C. D. Christofferson, P.-H. Chu, M. L. Clark, C. Cuesta, J. A. Detwiler, Yu. Efremenko, H. Ejiri, S. R. Elliott, G. K. Giovanetti, M. P. Green, J. Gruszko, I. S. Guinn, V. E. Guiseppe, C. R. Haufe, R. Henning, D. Hervas Aguilar, E. W. Hoppe, A. Hostiuc, M. F. Kidd, I. Kim, R. T. Kouzes, T. E. Lannen V., A. Li, A. M. Lopez, J. M. López-Castaño, E. L. Martin, R. D. Martin, R. Massarczyk, S. J. Meijer, S. Mertens, T. K. Oli, G. Othman, L. S. Paudel, W. Pettus, A. W. P. Poon, D. C. Radford, A. L. Reine, K. Rielage, N. W. Ruof, D. C. Schaper, D. Tedeschi, R. L. Varner, S. Vasilyev, J. F. Wilkerson, C. Wiseman, W. Xu, C.-H. Yu, and B. X. Zhu. Final result of the majorana demonstrator's search for neutrinoless double-β decay in ^{76}Ge. *Phys. Rev. Lett.*, 130:062501, Feb 2023. doi: 10.1103/PhysRevLett.130.062501. URL https://link.aps.org/doi/10.1103/PhysRevLett.130.062501.

[25] Laboratori Nazionali del Gran Sasso. Annual report. Technical report, Laboratori Nazionali del Gran Sasso, 2011.

[26] H. Acharya et al. First results on the search for lepton number violating neutrinoless double-β decay

with the legend-200 experiment. *Phys. Rev. Lett.*, pages –, Sep 2025. doi: 10.1103/25tk-nctn. URL https://link.aps.org/doi/10.1103/25tk-nctn.

[27] I. Abt, L. Garbini, C. Gooch, S. Irlbeck, X. Liu, M. Palermo, and O. Schulz. Alpha-event and surface characterisation in segmented true-coaxial hpge detectors. *Nuclear Instruments and Methods in Physics Research Section A: Accelerators, Spectrometers, Detectors and Associated Equipment*, 858:80–89, 2017. ISSN 0168-9002. doi: https://doi.org/10.1016/j.nima.2017.03.057. URL https://www.sciencedirect.com/science/article/pii/S0168900217304096.

[28] G F Knoll. *Radiation Detection and Measurement*. John Wiley and Sons,New York, NY, 1978.

[29] R.J. Cooper, D.C. Radford, P.A. Hausladen, and K. Lagergren. A novel hpge detector for gamma-ray tracking and imaging. *Nuclear Instruments and Methods in Physics Research Section A: Accelerators, Spectrometers, Detectors and Associated Equipment*, 665:25–32, 2011. ISSN 0168-9002. doi: https://doi.org/10.1016/j.nima.2011.10.008. URL https://www.sciencedirect.com/science/article/pii/S0168900211018985.

[30] LEGEND Collaboration, N. Abgrall, I. Abt, M. Agostini, A. Alexander, C. Andreoiu, G. R. Araujo, F. T. Avignone III, W. Bae, A. Bakalyarov, M. Balata, M. Bantel, I. Barabanov, A. S. Barabash, P. S. Barbeau, C. J. Barton, P. J. Barton, L. Baudis, C. Bauer, E. Bernieri, L. Bezrukov, K. H. Bhimani, V. Biancacci, E. Blalock, A. Bolozdynya, S. Borden, B. Bos, E. Bossio, A. Boston, V. Bothe, R. Bouabid, S. Boyd, R. Brugnera, N. Burlac, M. Busch, A. Caldwell, T. S. Caldwell, R. Carney, C. Cattadori, Y. D. Chan, A. Chernogorov, C. D. Christofferson, P. H. Chu, M. Clark, T. Cohen, D. Combs, T. Comellato, R. J. Cooper, I. A. Costa, V. D'Andrea, J. A. Detwiler, A. Di Giacinto, N. Di Marco, J. Dobson, A. Drobizhev, M. R. Durand, F. Edzards, Yu. Efremenko, S. R. Elliott, A. Engelhardt, L. Fajt, N. Faud, M. T. Febbraro, F. Ferella, D. E. Fields, F. Fischer, M. Fomina, H. Fox, J. Franchi, R. Gala, A. Galindo-Uribarri, A. Gangapshev, A. Garfagnini, A. Geraci, C. Gilbert, M. Gold, C. Gooch, K. P. Gradwohl, M. P. Green, G. F. Grinyer, A. Grobov, J. Gruszko, I. Guinn, V. E. Guiseppe, V. Gurentsov, Y. Gurov, K. Gusev, B. Hacket, F. Hagemann, J. Hakenmüeller, M. Haranczyk, L. Hauertmann, C. R. Haufe, C. Hayward, B. Heffron, F. Henkes, R. Henning, D. Hervas Aguilar, J. Hinton, R. Hodak, H. Hoffmann, W. Hofmann, A. Hostiuc, J. Huang, M. Hult, M. Ibrahim

Mirza, J. Jochum, R. Jones, D. Judson, M. Junker, J. Kaizer, V. Kazalov, Y. Kermaïdic, H. Khushbakht, M. Kidd, T. Kihm, K. Kilgus, I. Kim, A. Klimenko, K. T. Knöpfle, O. Kochetov, S. I. Konovalov, I. Kontul, K. Kool, L. L. Kormos, V. N. Kornoukhov, M. Korosec, P. Krause, V. V. Kuzminov, J. M. López-Castaño, K. Lang, M. Laubenstein, E. León, B. Lehnert, A. Leonhardt, A. Li, M. Lindner, I. Lippi, X. Liu, J. Liu, D. Loomba, A. Lubashevskiy, B. Lubsandorzhiev, N. Lusardi, Y. Müller, M. Macko, C. Macolino, B. Majorovits, F. Mamedov, W. Maneschg, L. Manzanillas, G. Marshall, R. D. Martin, E. L. Martin, R. Massarczyk, D. Mei, S. J. Meijer, S. Mertens, M. Misiaszek, E. Mondragon, M. Morella, B. Morgan, T. Mroz, D. Muenstermann, C. J. Nave, I. Nemchenok, M. Neuberger, T. K. Oli, G. Orebi Gann, G. Othman, V. Palušova, R. Panth, L. Papp, L. S. Paudel, K. Pelczar, J. Perez Perez, L. Pertoldi, W. Pettus, P. Piseri, A. W. P. Poon, P. Povinec, A. Pullia, D. C. Radford, Y. A. Ramachers, C. Ransom, L. Rauscher, M. Redchuk, A. L. Reine, S. Riboldi, K. Rielage, S. Rozov, E. Rukhadze, N. Rumyantseva, J. Runge, N. W. Ruof, R. Saakyan, S. Sailer, G. Salamanna, F. Salamida, D. J. Salvat, V. Sandukovsky, S. Schönert, A. Schültz, M. Schütt, D. C. Schaper, J. Schreiner, O. Schulz, M. Schuster, M. Schwarz, B. Schwingenheuer, O. Selivanenko, M. Shafiee, E. Shevchik, M. Shirchenko, Y. Shitov, H. Simgen, F. Simkovic, M. Skorokhvatov, M. Slavickova, K. Smolek, A. Smolnikov, J. A. Solomon, G. Song, K. Starosta, I. Stekl, M. Stommel, D. Stukov, R. R. Sumathi, D. A. Sweigart, K. Szczepaniec, L. Taffarello, D. Tagnani, R. Tayloe, D. Tedeschi, M. Turqueti, R. L. Varner, S. Vasilyev, A. Veresnikova, K. Vetter, C. Vignoli, C. Vogl, K. von Sturm, D. Waters, J. C. Waters, W. Wei, C. Wiesinger, J. F. Wilkerson, M. Willers, C. Wiseman, M. Wojcik, V. H. S. Wu, W. Xu, E. Yakushev, T. Ye, C. H. Yu, V. Yumatov, N. Zaretski, J. Zeman, I. Zhitnikov, D. Zinatulina, A. K. Zschocke, A. J. Zsigmond, K. Zuber, and G. Zuzel. Legend-1000 preconceptual design report, 2021. URL `https://arxiv.org/abs/2107.11462`.

[31] Matteo Agostini, Jason Detwiler, Luigi Pertoldi, Ian Guinn, George Marshall, Toby Dixon, Valerio D'Andrea, Patrick Krause, Grace Song, Erin Engelhardt, Sam Borden, Rosanna Deckert, David Sweigart, Andreas Zschocke, Clint Wiseman, Tim Mathew, Yoann Kermaïdic, and Ben Shanks. pygama, October 2025. URL `https://doi.org/10.5281/zenodo.17408227`.

[32] G. Othman. *The CAGE Scanner: Investigating Surface Backgrounds in High-Purity Germanium De-*

tectors. PhD thesis, University of North Carolina, Chapel Hill, 2021. URL https://doi.org/10.17615/y6x2-a646.

[33] Paul Barton, Paul Luke, Mark Amman, Yuen-Dat Chan, Jason Detwiler, James Loach, Ryan Martin, Alan Poon, Craig Tindall, and Kai Vetter. Low-noise low-mass front end electronics for low-background physics experiments using germanium detectors. In *2011 IEEE Nuclear Science Symposium Conference Record*, pages 1976–1979, 2011. doi: 10.1109/NSSMIC.2011.6154397.

[34] Mark Howe Mike Marino TJ Corona Jason Detwiler Mike Marino Alexis Schubert Andreas Kopmann Till Bergmann Jan Wouters Frank McGirt John F. Wilkerson, Tom Caldwell. Orca. URL http://orca.physics.unc.edu/orca/Orca_Help/Home.html.

[35] Jared Kofron Benjamin LaRoque Noah S. Oblath Walter Pettus Luis Saldana Matthew Sternberg Luiz de Vivieros Megan Wachtendonk Yadi Wang Christine Claessens, Mathieu Guigue. dragonfly, December 2019. URL https://github.com/project8/dragonfly/.

[36] Kou Oishi Sanshiro Enamoto. Slowdash, 2025. URL https://github.com/slowproj/slowdash.

[37] Feb 2024. URL https://www.ce.washington.edu/research/facilities/xray.

[38] J. Gruszko and on behalf of the Majorana Collaboration. Delayed charge recovery discrimination of passivated surface alpha events in p-type point-contact detectors. *Journal of Physics: Conference Series*, 888(1):012079, sep 2017. doi: 10.1088/1742-6596/888/1/012079. URL https://doi.org/10.1088/1742-6596/888/1/012079.

[39] I. Abt, F. Fischer, F. Hagemann, L. Hauertmann, O. Schulz, M. Schuster, and A. J. Zsigmond. Simulation of semiconductor detectors in 3d with solidstatedetectors.jl. *Journal of Instrumentation*, 16(08): P08007, 8 2021. doi: 10.1088/1748-0221/16/08/p08007. URL https://doi.org/10.1088/1748-0221/16/08/p08007.

[40] I. Abt, C. Gooch, F. Hagemann, L. Hauertmann, X. Liu, O. Schulz, and M. Schuster. Bayesian inference of high-purity germanium detector impurities based on capacitance measurements and machine-

learning accelerated capacitance calculations. *The European Physical Journal C*, 83(5), May 2023. doi: 10.1140/epjc/s10052-023-11509-8.

[41] E. Engelhardt. *A Novel Method of Surface Event Rejection in Point-Contact HPGE Detectors for Neutrinoless Double-beta Decay Experiments*. PhD thesis, University of North Carolina, Chapel Hill, 2025. URL https://doi.org/10.17615/c3ve-c676.